

Euler Technology Assessment for Preliminary Aircraft Design—Compressibility Predictions by Employing the Unstructured Grid USM3D Code

Tom A. Kinard and Pradeep Raj

Contract NAS1-19000
Prepared for Langley Research Center

March 1996



Euler Technology Assessment for Preliminary Aircraft Design—Compressibility Predictions by Employing the Unstructured Grid USM3D Code

Tom A. Kinard and Pradeep Raj
Lockheed Martin Aeronautical Systems • Marietta, Georgia

Printed copies available from the following:

NASA Center for AeroSpace Information
800 Elkridge Landing Road
Linthicum Heights, MD 21090-2934
(301) 621-0390

National Technical Information Service (NTIS)
5285 Port Royal Road
Springfield, VA 22161-2171
(703) 487-4650

TABLE OF CONTENTS

SUMMARY	1
INTRODUCTION	2
LIST OF SYMBOLS	4
ANALYSIS TOOLS	5
Grid Generation	5
Flow Solver	7
Postprocessing	7
GRID SENSITIVITY	8
TWIN-TAIL MODEL	9
Geometry and Grid	9
Flow Analysis	10
Symmetric Flow Results	12
Asymmetric Flow Results	14
CENTERLINE-TAIL MODEL	15
Geometry and Grid	15
Flow Analysis	16
Symmetric Flow Results	18
Asymmetric Flow Results	20
CONCLUSIONS AND SUGGESTIONS FOR FUTURE WORK	21
ACKNOWLEDGMENTS	23
REFERENCES	24
TABLES	25
FIGURES	28

EULER TECHNOLOGY ASSESSMENT FOR
PRELIMINARY AIRCRAFT DESIGN - COMPRESSIBILITY PREDICTIONS BY
EMPLOYING THE UNSTRUCTURED GRID USM3D CODE

Tom A. Kinard
Pradeep Raj

Lockheed Martin Aeronautical Systems

SUMMARY

This study has been conducted in support of a NASA project aimed at assessing the viability of using Euler technology to produce aerodynamic data for preliminary design. The primary objective is to evaluate the effectiveness of unstructured-grid techniques in simulating compressibility effects for vortical flows. The approach involves comparing computed subsonic- and transonic-flow solutions with each other and with experimental data for a twin-tail and a centerline-tail modular transonic vortex interaction (MTVI) model, representative of generic fighter configurations. The present effort is focused on the application of the unstructured tetrahedral-grid USM3D code. This code, developed at the NASA-Langley Research Center, employs a cell-centered finite-volume upwind algorithm with explicit or implicit time marching scheme to solve the inviscid compressible-flow Euler equations. In this report, correlations of USM3D solutions with measured data are presented at 0.4 and 0.85 Mach numbers for symmetric as well as asymmetric flow conditions. For symmetric cases, the angle of attack varies from 10° to 30° ; asymmetric cases cover side-slip angles of 2° , 4° and 7° at selected angles of attack. The results show that Euler solutions can provide meaningful guidelines for preliminary design of flight vehicles which exhibit vortex flows in parts of their flight envelope.

INTRODUCTION

Advanced fighter aircraft must be designed to meet stringent performance requirements over a wide range of angle-of-attack and Mach number conditions. The design process can be greatly helped if aerodynamic characteristics associated with moderate-to-high angles of attack can be simulated in an *accurate*, *cost-effective* and *timely* manner using computational fluid dynamics (CFD). Vortices generally dominate aerodynamic characteristics of fighter aircraft at higher angles of attack. In late 1993, NASA-Langley Research Center (LaRC) initiated a collaborative study with U.S. aerospace industry. The study was aimed at assessing the viability of using state-of-the-art CFD Euler technology, i.e., CFD methods that solve the inviscid, compressible-flow Euler equations, for producing aerodynamic data to satisfy the preliminary design needs. During the first phase of the study, carried out in FY '94, both structured-grid (TEAM and OVERFLOW) and unstructured-grid (SPLITFLOW and USM3D) codes were evaluated. The results are documented in references 1, 2 and 3. It could be concluded from the results that the unstructured-grid technology, although less mature than the structured-grid, was better suited to meeting the preliminary-design needs.

The present phase of the study involves just further evaluation of the promising codes selected from the first phase, SPLITFLOW and USM3D. The first code represents the state of the art in unstructured Cartesian-grid techniques and the second in tetrahedral grids. The principal objective is to evaluate the effectiveness of these methods in simulating compressibility effects for vortex-dominated flows. The approach involves exercising each code on two modular transonic vortex interaction (MTVI) models with different vertical tail arrangement, one with centerline tail and the other with twin tails. The overall geometric features are shown in figure 1. The aerodynamic characteristics of these

models are dominated by two primary vortices. The first one emanates from the chine on the forebody and travels down the body on the leeward side. The second vortex results from flow separation along the sharp leading edge of the wing and travels downstream close to the wing leading edge. The interaction of the chine and wing vortices with one another and neighboring aerodynamic surfaces, influence the overall configuration aerodynamic characteristics in a significant way.

The USM3D results obtained by Lockheed Martin Aeronautical Systems (LMAS) are documented in this report. A companion report prepared by Lockheed Martin Tactical Aircraft Systems (LMTAS) contains the SPLITFLOW results. The grid used for USM3D analyses was selected on the basis of a grid sensitivity investigation using the centerline-tail model as discussed later on in this report. The report contains comparisons of computed and measured forces, moments, and surface pressure for the flow conditions shown in Table 1. Surface pressure correlations are presented for six cross-plane stations, three on the forebody and three on the aft-fuselage and wing; the stations are shown in figure 2. All experimental data supplied by LaRC [4] was previously generated in a 7' x 10' wind-tunnel test. Estimates of problem set-up time and computer resources are also included herein. The report concludes with suggestions for future work.

LIST OF SYMBOLS

b	span
c_{ref}	mean aerodynamic chord
CFL	Courant-Friedrichs-Lewy number
C_p	coefficient of pressure
C_D	drag coefficient
C_L	lift coefficient
C_Y	side force coefficient
C_m	pitching-moment coefficient
C_n	yawing-moment coefficient
C_r	rolling-moment coefficient
M	free-stream Mach Number
Re	Reynolds number
S_{ref}	reference area
x,y,z	body-fixed Cartesian coordinate system: x positive along model axis, y positive from symmetry plane to wing tip (starboard), and z positive up
α	angle of attack
β	side-slip angle

ANALYSIS TOOLS

In this section, software and hardware tools used in the present investigation are discussed; results obtained by applying these tools to the MTVI models are presented in the following sections. These tools were required to generate grids, to produce flow solutions, and to extract the desired aerodynamic data from the solutions. Only basic features of the tools are highlighted here. Appropriate references are cited for readers interested in more details. The bulk of grid generation and solution postprocessing was carried out on Silicon Graphics workstations and the solutions were produced using the Cray C-90 supercomputer of the NASA Numerical Aerodynamic Simulation (NAS) facility.

Grid Generation

The analysis process started with the configuration geometry files supplied by NASA [4]. Tetrahedral grids were generated using a NASA-Langley software system composed of two codes: GridTool and VGRID. GridTool [5] accepts geometry files in either discrete point or IGES [6] format. Once a geometry file is entered into the program, a user interactively constructs curves and patches on the surfaces exposed to the flow. When the entire surface has been divided into patches, the outer boundaries are set up usually as a simple box. Point and line sources are then prescribed which control the distribution of points not only on the surface but also in the field. A restart option is available to allow the user to save intermediate results. This option is particularly helpful in treating complex configurations which may require more than one session to complete the patching. GridTool also has the capability of displaying surface grids on a patch-by-patch basis to allow the user to inspect the quality of an unstructured surface mesh. The output of GridTool is an

input file for VGRID.

VGRID [7] is used to generate the surface and volume grids. This code uses the advancing front method for grid generation. A structured background mesh[8] is used to control the point distribution for both surface and volume grids. The background mesh is constructed by subdividing the entire flow domain into cells. Spacing information needed to control distribution of tetrahedra is stored at the nodes of the cells. The grid spacing distributions are determined in a manner similar to the diffusion of heat in a conducting medium from discrete sources.

Once the background mesh has been created a surface grid is constructed by placing points along the edges of the user defined patches which form the initial front to triangulate the entire patch. After each patch is triangulated, the surface grid quality is checked automatically and any regions of poor quality are displayed. The user has the ability to change the patch in order to achieve a better grid as necessary. The surface grid then forms the initial front for the volume grid. The front is advanced into the field by introducing new points and forming tetrahedra and new faces to complete the grid. This step is usually accomplished in a batch process. The code continues to fill the flowfield domain until either the domain is completely filled or no more cells can be formed thus leaving pockets or voids. These pockets are then filled by removing a layer of cells around the pocket creating a larger void and a new front. The grid generator is restarted and cells are added until the grid is completed. In some cases the point and line sources have to be modified in order to achieve an acceptable grid. A grid quality check is then initiated. Cells with negative volumes and/or high skewness are identified. A few cells around the bad cell are removed and the region is refilled. Once an acceptable grid has been generated, the next step is to compute the flow solution using the Euler solver, USM3D.

Flow Solver

The USM3D [9] flow solver, developed at NASA Langley, solves the time-dependent compressible-flow Euler equations for an ideal gas using a cell-centered finite volume formulation. Spatial discretization is based on Roe's flux-difference [10] or flux-vector splitting [11]. The solutions are advanced in time by either an explicit multi-stage Runge-Kutta scheme or an implicit Gauss-Seidel scheme. Local time stepping is used to accelerate convergence to a steady state by advancing the flow variables in time for each cell with a CFL number near the local stability limit. The maximum time step for the explicit scheme is enlarged by the use of implicit residual smoothing. USM3D supports boundary conditions commonly available in Euler solvers.

Although the code was run on Cray C-90 for the present work, it can easily be run on high-end workstations with sufficient memory and computing speed. The code uses 43 words per cell of core memory and 14.5 μ sec per cell per cycle for the explicit scheme and 180 words per cell of core memory and 29 μ sec per cell per cycle for the implicit scheme. The computer times apply to a Cray C-90 run.

Postprocessing

FAST [12] and VPLOT3D [7] were the two principal software tools used to postprocess the flow solutions in order to generate the desired on and off-body flow quantities. The ACE/gr software package [13] was used for producing x-y type plots such as convergence histories and surface pressure correlations.

GRID SENSITIVITY

One of the first tasks undertaken in this effort was to conduct a grid sensitivity study in order to select a "suitable" grid for accurately capturing flow features associated with the range of pitch and yaw angles under consideration (see Table 1). This study involved generating four grids on the MTVI centerline-tail model, obtaining flow solutions on each grid at $M = 0.4$ and $\alpha = 20^\circ$, and comparing the computed solutions with each other and with experimental data.

The results of this study are summarized in table 2. The table includes: (1) relevant grid parameters for each grid, namely, number of cells, NCELL, number of nodes, NNODE, number of boundary points, NBTPS, number of boundary faces, NBFACE, and total number of faces, NTFACE, (2) values of computed lift, drag and pitching moment coefficients, (3) computer resources needed to carry out the analyses such as run time and memory, and (4) convergence levels achieved on each grid. Grid parameters were controlled by varying the strengths of the line sources uniformly throughout the flow field. Typical convergence histories for the finest-grid analysis are shown in figure 3; other grids exhibited very similar behavior. For all analyses, the implicit scheme was used with the CFL number set at 75. All computations were obtained using flux difference splitting.

Correlations of computed surface pressure distributions with experimental data at six crossplane stations are shown in figure 4. An examination of the force, moment, and pressure data shows that with increasing number of cells, the differences between the successive set of computed results decreases. In general, the computed surface pressure characteristics were adequately predicted by all four grids. Grid 3 was considered to offer the best balance between accuracy and computational efficiency. Therefore, it was selected and then used to analyze all cases on the centerline-tail model. A perspective view of surface and plane-of-symmetry grid is

shown in figure 5. The grid also served as a guide for building a grid on the twin-tail model that is shown in figure 6.

TWIN-TAIL MODEL

In this section, the results of MTVI twin-tail model analysis are discussed. The section is divided into four subsections. Relevant details of configuration geometry and grid generation are presented first. A summary of the analysis process follows in the second subsection. Correlations of computed solutions with measured data for symmetric and asymmetric flow cases are presented in the last two subsections.

Geometry and Grid

A perspective view of the surface geometry of the twin-tail MTVI model is shown in figure 1. The model has a chined forebody with an included angle of 30° and a cropped-delta wing with 60° leading-edge sweep and 1.8 aspect ratio. The entire configuration is made up of analytically defined components. The wing airfoil section is biconvex whereas the vertical-tail section is a thin diamond shape. All edges of the wing and tail surfaces are sharp.

As mentioned in the previous section, GridTool and VGRID were used for grid generation. Starting from the IGES surface geometry file supplied by NASA [4], the entire surface was divided into 92 patches using GridTool. Line sources were placed along the chine and the perimeter of the wing as well as along the wing root in order to cluster points in these regions. The vertical tail also had line sources along the leading and trailing edges and the tip. In addition, a line source was placed inside

of the (non-metric sting i.e. the sting provided no contribution to the overall forces or moments). For improved vortical-flow resolution, one source was placed along a line connecting the forward wing/body junction point with the trailing edge at approximately two-thirds span. The resulting surface grid contained 38,640 triangles and 19,322 nodes. The volume grid had 821,553 tetrahedral cells and 150,150 nodes. A partial view of the grids on the surface and the plane of symmetry is shown in figure 6. It took approximately 8 to 10 labor hours to generate the grid. The grid for asymmetric cases was generated by reflecting the half-model grid about the longitudinal plane of symmetry resulting in a grid with 1,248,464 cells. Note that the half-model grid used for symmetric-flow analysis was somewhat coarsened before a full-model grid was built. This was done because of a memory restriction on the computing resource, but the solutions were not affected in a significant way.

Flow Analysis

In this subsection, some general observations are made about the USM3D analysis of the MTVI twin-tail model. A total of 20 runs were made. As shown in table 1, a set of 14 runs was for symmetric flow conditions ($\beta = 0$) and the remaining 6 for asymmetric flow conditions ($\beta \neq 0$) at a fixed α of 25° . In each set, half the runs were for subsonic (0.4) Mach number and half for transonic (0.85). The prioritized order of the runs is shown in table 3. For each run, a case number is shown in the second column that identifies the associated experimental data base of forces, moments and surface pressures. The flow conditions are given in columns 3 and 4. Typical computer times were of the order of 3 hours of Cray C-90 for symmetric-flow conditions and about twice as much for the asymmetric ones. Approximately 150 megawords (MW) of memory was required for symmetric-flow analyses and about 225 MW for the asymmetric ones.

All runs were made using the implicit time marching scheme. The scheme, as implemented in USM3D, starts the analysis process with one value of CFL number (cfl1) and incrementally ramps it up to a higher value (cfl2) over a prescribed number of cycles (iramp). This strategy is intended to enhance robustness of the solution process. Many times, it is sufficient to set cfl1 and cfl2 to the same value (with iramp set to zero) which keeps the CFL number fixed for the entire solution process. The combination of values used for each run are listed in table 3. The table also shows the total number of cycles for each run and the order of magnitude reduction in root-mean-square (rms) residual. Although various combinations of CFL numbers were utilized to obtain solutions, the scope of the project did not allow for a systematic study to determine an "optimum" CFL number for each run.

In general, the code was found to be more robust for subsonic analyses than for transonic. For example, relatively higher values of CFL number could be used for subsonic cases as compared to transonic. The subsonic analyses could be carried out without using flux limiters whereas either minmod or superbee limiters had to be invoked for transonic-flow analyses. Also, nearly all subsonic-flow cases were run using the built-in switching operation (iorder = 0) where the solution process starts with a first-order spatial discretization scheme and automatically switches to second order after approximately one order of magnitude reduction in rms residual. For transonic cases, and especially at higher angles of attack, the code had to be run first using first-order discretization (iorder = 1) until the residual dropped by two or three orders of magnitude and then the process was restarted with second-order discretization (iorder = 2).

The levels of residual reduction were quite dependent on the flow conditions. Although nearly three orders of magnitude reduction was achieved for subsonic low- α runs, close to one order of magnitude reduction was the norm for most runs, and even less than that for some as shown in table 3. Note that the small levels of

residual reduction reflect the solution process settling into an oscillatory pattern with the residual (as well as force and moment values) oscillating about a mean. The solution was not diverging but it was not converging either. The oscillatory pattern could be attributed to localized regions of unsteady flow over the aft portions of the wing. The unsteadiness resulted from vortex interactions with the vertical tail for subsonic cases and with the tail and shock waves for transonic cases leading to vortex instabilities. Such interactions could be discerned from examining the surface-pressure distributions and more readily from observing the off-body flow features. A comparison with the corresponding data for the centerline tail model (table 4) further substantiates the role of vortex/tail interactions. Lower levels of rms residuals were generally achieved for the centerline tail model which does not experience such interactions.

Symmetric Flow Results

The symmetric-flow results corresponding to 0.4 and 0.85 Mach numbers at seven angles of attack, namely, 10, 12.5, 15, 17.5, 20, 25, and 30 degrees, are presented in this section. The results include force and moment data comparisons as well as surface pressure correlations for the twin tail configuration.

In figure 7, the computed and measured force and moment coefficients for both subsonic ($M = 0.4$) and transonic ($M = 0.85$) conditions are shown. For the entire range of α 's, the compressibility effects in the test data, manifest themselves as higher values of C_L for transonic Mach number as compared to subsonic. This trend is fairly well captured by the computed solutions for α 's up to 20° but not so well for the higher α 's. A break in the slope of the C_L - α curve between 12.5 and 17.5 degrees of α is another notable feature of the test data. The computed solutions faithfully capture this trend as well as those seen in C_L - C_D and C_L - C_m data of figure

7.

The following set of seven figures, one for each of the seven angles of attack, illustrate the compressibility effects on surface pressure distributions. Each figure compares computed and measured surface C_p 's at six cross-plane stations (shown in figure 2). In general, the computed results follow the trends exhibited by the measured data. For example, the transonic flow solutions show reduced suction peaks which are associated with leading edge vortex flows compared to the subsonic solutions consistent with the trends of the measured data. The computations also predict vortex bursting somewhere between the last two stations above the wing for all α 's greater than 12.5° . This vortex bursting phenomenon causes the shifts in test data in figure 7.

Overall, the computed values correlate fairly well with the measured values but many areas of discrepancies can be seen. The most noticeable one is on the very first forebody station where the computed solutions do not capture the C_p peak exhibited by experimental data. For some of the runs, the computed locations and magnitudes of C_p peaks on the aftbody/wing stations differ from the measured values. Discrepancies may be partly attributed to the lack of viscous effects in the present analysis. Inadequacy of the grid to fully resolve the flow features may be another factor that needs further investigation.

The complex nature of the flow resulting from interactions¹ of chine and wing vortices and from vortex interaction with tail (and shock waves in transonic flows) presents quite a challenge for the USM3D code. Figures 15 through 17 illustrate this flow complexity for one sample case of 20° angle of attack. In figures 15 and 16, the off-body distributions of total pressure are shown at six cross-plane stations. The view in these two figures is from a fixed point forward of the nose looking downstream along the x-axis. They clearly show the mutual interaction of chine and wing vortices and the eventual bursting near the vertical tail. Note that the total

pressure levels for the transonic solutions were lower than 0.7 but 0.7 was selected as the lower bound of the scale. This decision was dictated by the need to compare the subsonic and transonic solutions using a common scale. Smaller values of the lower bound led to significant loss of detail in the subsonic solutions. For each station, a comparison of the subsonic solution in the left column with the transonic solution on the right shows the significant effect of compressibility on the vortical flow features. The associated surface C_p contours are presented in figure 17.

Asymmetric Flow Results

Results for six runs are presented in this section. Three of them correspond to 0.4 Mach number and side-slip angles of 2° , 4° , and 7° . The other three have the same side-slip angles but 0.85 Mach number. For all runs the angle of attack is 25° . In figure 18, the compressibility effects on C_m - β , C_r - β and C_n - β curves are shown. With the exception of the rolling moment coefficient, there are relatively large discrepancies between the computed results and measured data. The discrepancies can be traced to differences between computed and measured surface pressures, especially on the upper surface of the wing on the windward side as shown in figures 19 through 21. How much of the difference was caused by a lack of viscous effects in the analysis and how sensitive the results might be to grid distribution are questions that remain unresolved at this time.

The complex nature of the asymmetric flow and the effect of compressibility are illustrated in figures 22 through 24 for the 4° side-slip case. In figures 22 and 23, the off-body distributions of total pressure are shown at six cross-plane stations; the view is looking downstream along the x-axis from a point ahead of the nose. They clearly show differences in flow field on the starboard and port sides in regards to mutual interaction of vortices and the interaction of vortices with the

vertical tails. For each station, a comparison of the subsonic solution in the left column with the transonic solution on the right shows the significant effect of compressibility on the vortical flow features. The associated surface C_p contours are presented in figure 24.

CENTERLINE-TAIL MODEL

In this section, the results of MTVI centerline-tail model analysis are discussed. The section is divided into four subsections. Relevant details of configuration geometry and grid generation are presented first. A summary of the analysis process follows in the second subsection. Correlations of computed solutions with measured data for symmetric and asymmetric flow cases are presented in the last two subsections.

Geometry and Grid

A perspective view of the surface geometry of the centerline-tail MTVI model is shown in figure 1. The model has a chined forebody with an included angle of 30° and a cropped-delta wing with 60° leading-edge sweep and 1.8 aspect ratio. The entire configuration is made up of analytically defined components. The wing airfoil section is biconvex whereas the vertical-tail section is a thin diamond shape. All edges of the wing and tail surface are sharp.

As mentioned earlier, the GridTool and VGRID software packages were used for grid generation. Starting from the IGES surface geometry file supplied by NASA[4], the entire surface was divided into 92 patches using GridTool. Line sources were placed along the chine, the perimeter of the wing, and along the wing

root in order to cluster points in these regions. The vertical tail also had line sources along the leading and trailing edges and the tip. In addition, a line source was placed inside of the (non-metric) sting. For improved vortical-flow resolution, one source was placed along a line connecting the forward wing/body junction point and the trailing edge at two-thirds span. The resulting surface grid contained 38,852 triangles and 19,428 nodes. The volume grid had 613,826 tetrahedral cells and 114,470 nodes. A partial view of the grids on the surface and the plane of symmetry is shown in figure 6. It took approximately 8 to 10 labor hours to generate the grid. For asymmetric cases, the grid was reflected about the longitudinal plane of symmetry resulting in a grid with 1,227,652 cells.

Flow Analysis

In this subsection, some general observations are made about the USM3D analysis of the MTVI centerline-tail model. A total of 22 runs were planned. As shown in table 1, a set of 10 runs was for symmetric flow conditions ($\beta = 0$) and the remaining 12 for asymmetric flow conditions ($\beta \neq 0$), six each for α of 15° and 25° . In each set, half the runs were for subsonic (0.4) Mach number and half for transonic (0.85). The prioritized order of the runs is shown in table 3. For each run, a case number is shown in the second column that identifies the associated experimental data base of forces, moments and surface pressures. The flow conditions are given in columns 3 and 4. Note that solutions could not be obtained for two transonic asymmetric-flow conditions, runs 16 and 22, because the solution process diverged. Typical computer times for the symmetric-flow runs were of the order of 3 hours and about twice as much for the asymmetric-flow runs. The corresponding memory requirements were 110 MW for symmetric-flow analyses and 225 MW for asymmetric-flow.

All runs were executed using schemes consistent with the twin tail analysis. The combination of values used for each run are listed in table 4. The table also shows the total number of cycles for each run and the order of magnitude reduction in rms residual. Although various combinations of CFL numbers were utilized to obtain solutions, the scope of the project did not allow for a systematic study to determine an "optimum" CFL numbers for each case.

In general, experiences with USM3D application to the centerline-tail model were similar to those for the twin-tail model. The code was found to be more robust for subsonic analyses than for transonic. For example, relatively higher values of CFL number could be used for subsonic cases as compared to transonic. The subsonic analyses could be carried out without using flux limiters whereas either minmod or superbee limiters had to be invoked for transonic-flow analyses. Also, nearly all subsonic-flow cases were run using the built-in switching operation ($iorder = 0$) where the solution process starts with a first-order spatial discretization scheme and automatically switches to second order after approximately one order of magnitude reduction in rms residual. For transonic cases, and especially at higher angles of attack, the code had to be run first using first-order discretization ($iorder = 1$) until the residual dropped by two or three orders of magnitude and then the process was restarted with second-order discretization ($iorder = 2$).

The levels of residual reduction were somewhat dependent on the flow conditions. For subsonic and transonic symmetric-flow conditions, three or more orders of magnitude reduction was achieved for most of the runs with the exception of runs 5 and 10 corresponding to $\alpha = 30^\circ$. For run 5 ($M = 0.4$), the solution process settled into an oscillatory pattern with the residual (as well as force and moment values) oscillating about a mean. The solution convergence characteristics exhibited a limit cycle i.e. the solution was not diverging or converging. The oscillatory pattern could be traced to regions of unsteady flow over the aft portions

of the wing resulting from vortex bursting. For run 10 ($M = 0.85$), the solution residual dropped only 0.6 orders with little change in force and moment values after about 250 cycles. For asymmetric-flow conditions, robust convergence characteristics were observed for both subsonic and transonic Mach numbers for the 15° angle-of-attack runs. However, the 25° angle-of-attack run's residual dropped one to two orders of magnitude and then followed a limit cycle pattern. This limit cycle pattern could be attributed to regions of unsteady flow on the aft portions of the wing associated with the onset of vortex instabilities or bursting. The unsteady-flow regions could be discerned from examining the surface-pressure distributions and more readily from observing the off-body flow features.

Symmetric Flow Results

The symmetric-flow results are presented in this section. They correspond to 0.4 and 0.85 Mach numbers and five angles of attack, namely, 10, 15, 20, 25, and 30 degrees. The results include force and moment data comparisons as well as surface pressure correlations.

In figure 25, the computed and measured force and moment coefficients for both subsonic ($M = 0.4$) and transonic ($M = 0.85$) conditions are shown. The compressibility effects in the test data, manifest themselves as higher C_L values for transonic Mach number as compared to subsonic up to 20° angle of attack and lower values past that. The measured C_D values are slightly lower for the transonic Mach number as compared to subsonic for C_L 's up to about 1.1 and higher for larger C_L 's. The measured pitching-moment coefficients are consistently more negative for the entire range of C_L 's. These trends are fairly well captured by the computed solutions except for the 30° angle-of-attack runs for which the computed values deviate substantially from the measured data.

The following set of five figures illustrate the compressibility effects on surface pressure distributions for each of the five angles of attack. In each figure computed and measured surface C_p 's are compared at six cross-plane stations (shown in figure 2). In general, the computed results follow the trends exhibited by the measured data. For example, the transonic flow solutions show reduced suction peaks, which are associated with leading edge vortex flows, compared to the subsonic solutions. Overall, the computed values correlate fairly well with the measured values but many areas of discrepancies can be seen. Similar to the twin tail MTVI results, the most noticeable one is on the very first forebody station where the computed solutions do not capture the C_p peaks exhibited by the measured data. In addition, the computed locations and magnitudes of C_p peaks on some of the aft-body/wing stations differ from the measured values. The largest difference can be seen on the aftmost station for the $\alpha = 30^\circ$ case which explains deviations in the force and moment data in figure 25. Discrepancies in surface pressure distributions may be partly attributed to the lack of viscous effects in the present analysis. Inadequacy of the grid to fully resolve the flow features may be another factor that needs further investigation.

The complex nature of the flow—resulting from interacting forebody and wing vortices (and vortices with shock waves in transonic flows)—presents quite a challenge for the present computational effort. Figures 31 through 33 illustrate this flow complexity for one sample case of 20° angle of attack. In figures 31 and 32, the off-body total pressure distributions are presented at six cross-plane stations. The view in these two figures is from a fixed point forward of the nose looking downstream along the x-axis. They clearly show the mutual interaction of chine and wing vortices as well as substantial effects of compressibility on flow features. Note that the total pressure levels for the transonic solutions were lower than 0.7 although 0.7 appears as the lower bound on the scale. Selecting 0.7 as the lower

bound was dictated by the need to have a common scale for comparing the subsonic and transonic solutions. When a smaller value was picked for the lower bound, it caused significant loss of detail in the subsonic solutions. In figure 33, the associated surface C_p contours are presented which show substantial differences caused by different vortical flow structures due to compressibility.

Asymmetric Flow Results

Two sets of results are presented in this section. The first set corresponds to $\alpha = 15^\circ$ and the second to $\alpha = 25^\circ$. Each set includes subsonic ($M = 0.4$) data for $\beta = 2^\circ, 4^\circ$, and 7° , and transonic ($M = 0.85$) data for $\beta = 2^\circ$ and 4° . In figure 34, the compressibility effects on C_m - β , C_r - β and C_n - β are shown for the lower α case. There are relatively large discrepancies between the computed results and measured data. The discrepancies can be traced to differences between computed and measured surface pressures, especially on the upper surface of the wing on the windward side as shown in figures 35 and 36. Similar results for the higher α case are in figures 37 through 39 (see figures 18 through 21 for a direct comparison with the twin-tail results). How much of the discrepancy was caused by a lack of viscous effects in the analysis and how sensitive the results might be to grid distribution are questions that remain unresolved at this time. These solutions show better correlation with data than the twin tail solutions.

The complex nature of the asymmetric flow and the effect of compressibility are illustrated in figures 40 through 42 for the 4° side-slip case. In figures 40 and 41, the off-body distributions of total pressure are shown at six cross-plane stations; the view is looking downstream along the x-axis from a point ahead of the nose. They clearly show differences in flow field on the starboard and port sides in regards to mutual interaction of vortices. For each station, a comparison of the

subsonic solution in the left column with the transonic solution on the right shows the significant effect of compressibility on the vortical flow features. The associated surface C_p contours are presented in figure 42.

CONCLUSIONS AND SUGGESTIONS FOR FUTURE WORK

The results of this study contribute to assessing the viability of using current state-of-the-art unstructured-grid Euler methods in preliminary design of aircraft configurations with sharp edges. Inviscid Euler solutions were obtained using the tetrahedral-grid USM3D code on twin-tail and centerline-tail MTVI models. The solutions were compared with test data to develop a better understanding of the capabilities of the code in accurately capturing the effects of compressibility for vortex-dominated flows. The results show that

- (a) The unstructured tetrahedral-grid Euler code, USM3D, Version 4.3, is more robust for modeling vortex flows at subsonic rather than transonic Mach numbers. The added complexity of vortex/shock interaction at transonic flows is the most likely cause.
- [b] The computed forces and moments for symmetric flow conditions generally follow the trends of the measured data; larger discrepancies are seen at asymmetric-flow conditions.
- [c] The forebody surface pressures tended to agree reasonably well (expected trends consistent with inviscid computations) with test data. The aftbody/wing pressures agreed well at low angles of attack but showed a larger deviation at higher angles of attack.
- (d) The integrated forces and moments as well as the overall flow features predicted by Euler methods may adequately meet the requirements of a

traditional preliminary-design environment but the use of Euler methods for design optimization must be approached with caution because the predicted distributed on- and off-body flow characteristics may not be of sufficient accuracy.

As is true with most research studies, the present study answered many questions and raised many new ones that could not be fully addressed due to schedule and resource constraints. We recommend that further investigation along the lines suggested below be conducted to resolve these issues:

- 1) A solution adaptive grid technique be incorporated into the code to accurately assess solution sensitivity to grid variations. Without such a technique, it will be extremely expensive and time consuming to efficiently capture the complex nature of the vortical flows encountered in this study because very fine field grids will be needed to resolve regions of high gradients associated with the vortices and shock waves.
- 2) A more comprehensive analysis of the solutions generated to date be performed to examine the various on and off-body flow quantities in much more detail. The analysis would include examination of separation and attachment lines on the surface, location and strength of vortices, vortex break-down, etc.
- 3) Viscous solutions be obtained at selected combinations of angles of attack and side-slip angles. The flow conditions of particular interest are those where the computed solutions deviate substantially from the measured data. Time-accurate analysis of burst vortex flows using the implicit time-marching scheme will also be of great interest.
- 4) The present study be extended to investigate the capabilities of the code to accurately predict the effects of forebody shaping. Application of the code for evaluating different geometries with respect to their aerodynamic performance is one area where its pay-offs can be most readily realized in preliminary design.

ACKNOWLEDGMENTS

The present study was conducted under contract no. NAS1-19000 sponsored by the Transonic/Supersonic Aerodynamics Branch, NASA-Langley Research Center, Hampton, Virginia, with Farhad Ghaffari as the Technical Monitor. Tom Kinard was the Principal Investigator and Dr. Pradeep Raj served as the Program Manager. Sabine Vermeersch provided substantial assistance in post-processing of the computed solutions. The LMAS team would like to thank Farhad Ghaffari and Dr. Neal Frink of NASA-LaRC for their invaluable support and cooperation during the performance of the contract. We gratefully acknowledge the NAS computer resources supplied by NASA. Special thanks are due to Dr. James M. Luckring, Head, Transonic/Supersonic Aerodynamics Branch, for giving us the opportunity to participate in this project.

Aerodynamics Department

Lockheed Martin Aeronautical Systems

Marietta, Georgia 30063

October 30, 1995

REFERENCES

1. Kinard, T.A., Harris, B.W., and Raj, P., "An Assessment of Viscous Effects in Computational Simulation of Benign and Burst Vortex Flows on Generic Fighter Wind-Tunnel Models Using TEAM Code," NASA CR 4650, March 1995.
2. Treiber, D.A. and Muilenburg, D.A., "Euler Technology Assessment for Preliminary Aircraft Design Employing OVERFLOW Code With Multiblock Structured-Grid Method," NASA CR 4651, March 1995.
3. Finley, D.B., "Euler Technology Assessment Program for Preliminary Aircraft Design Employing SPLITFLOW Code With Cartesian Unstructured Grid Method," NASA CR 4649, March 1995.
4. Ghaffari, F., NASA-Langley Research Center, personal communication, 1995.
5. Abolhassani, J., "GridTool: A Surface Modeling and Grid Generation Tool," NASA CP-3291, May 1995, pp. 821-832.
6. "The Initial Graphics Exchange Specification (IGES) Version 5.0," Distributed by National Computer Association, Administrator, IGES/PDES Organization, 2722 Merrilee Drive, Suite 200, Fairfax, VA 22031.
7. Parikh, P., Pirzadeh, S., and Löhner, R., "A Package for 3-D Unstructured Grid Generation, Finite-Element Flow Solution, and Flow Field visualization," NASA CR-182090, September 1990.
8. Pirzadeh, S., "Structured Background Grids for Generation of Unstructured Grids by Advancing Front Method," AIAA-91-3233, 1991.
9. Frink, N.T., Parikh, P., and Pirzadeh, S., "A Fast Upwind Solver for the Euler Equations on Three-dimensional Unstructured Meshes," AIAA 91-0102, January 1991.
10. Roe, P.L., "Characteristic-Based Schemes for the Euler Equations." *Annual Review of Fluid Mechanics*, Vol18, 1986, pp. 337-365.
11. Van Leer, B., "Flux-Vector Splitting for the Euler Equations," ICAS Report No. 82-30, September 1982; also Lecture Notes in Physics, Vol. 170, 1982, pp. 501-512.
12. Walatka, P.P., Clucas, J., McCabe, K., Plessel, T. and Potter, R., "FAST User Guide," RND-92-015, NASA-Ames Research Center, Moffett Field, California, November 1992.
13. Turner, P.J., "ACE/gr User's Manual," Center for Coastal and Land-Margin Research, Oregon Graduate Institute of Science and Technology, Beaverton, Oregon, 97006-1999, 1993.

Table 1. Run Matrix with Flow Conditions

Model	Mach Number	Angle of Attack α	Side-slip Angle β	No. of Runs
Twin Tail	0.4, 0.85	10, 12.5, 15, 17.5, 20, 25, 30	0	14
		25	2, 4, 7	6
Centerline Tail	0.4, 0.85	10, 15, 20, 25, 30	0	10
		15, 25	2, 4, 7	12

Table 2. Results of Grid Sensitivity Study

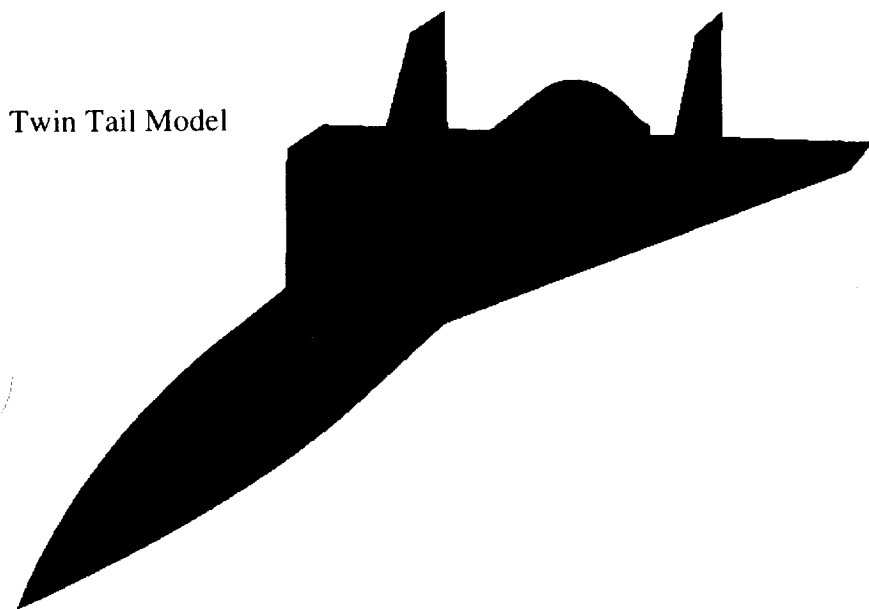
MTVI CENTERLINE TAIL MODEL M = 0.4, α = 20, β = 0 Test Data: CL = 1.14 CD = 0.411 CM = -0.0627				
	Grid 1	Grid 2	Grid 3	Grid 4
NCELL	405,815	529,425	613,826	714,392
NNODE	76,604	99,149	114,470	132,703
NBTPS	14,796	17,650	19,428	21,503
NBFACE	29,588	35,296	38,852	43,002
NTFACE	826,424	1,076,498	1,247,078	1,450,285
CL	1.2135	1.2223	1.2248	1.2263
CD + CD0	0.4459	0.4492	0.4500	0.4505
CM	-0.0916	-0.0949	-0.096	-0.0966
RUN TIME (seconds)	3565	4758	5442	6444
MEMORY (MW)	74	96	110	129
CYCLES	300	300	300	300
RESIDUAL REDUCTION (order of magnitude)	4.7	4.10	3.9	3.80

Table 3. Twin Tail Model USM3D Analysis

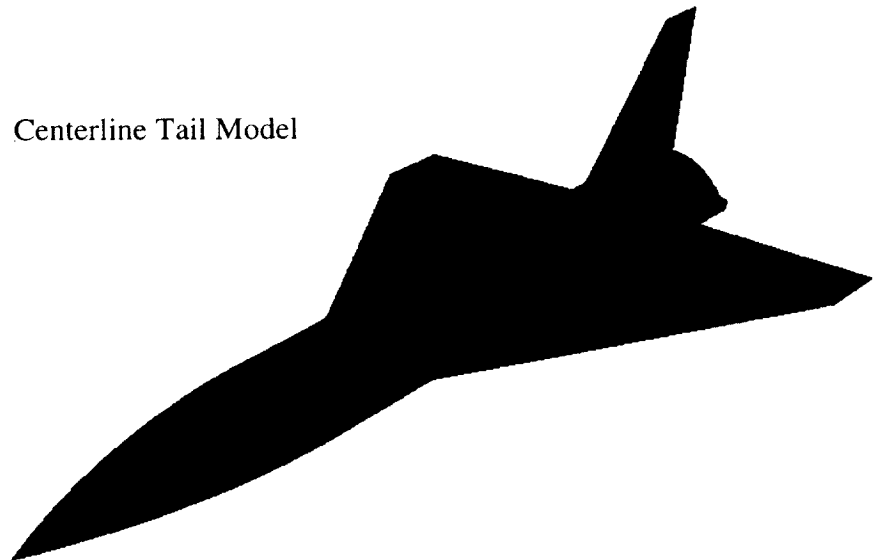
Run	Case (Exptl)	α/β	M	Cycles	Residual Reduction	cfl1	iramp	cfl2	Comments
1	3	10 / 0	0.4	400	2.6	75	0	75	
2	3	15 / 0	0.4	400	1.3	20	100	50	
3	3	20 / 0	0.4	700	1.0	75	0	75	
4	3	25 / 0	0.4	600	0.8	50	0	50	
5	3	30 / 0	0.4	600	0.9	50	0	50	
6	4	10 / 0	0.85	500	1.4	5	200	20	superbee
7	4	15 / 0	0.85	600	0.3	15	0	15	superbee
8	4	20 / 0	0.85	200		7	0	7	Initial (1st order)
				+200	0.3	7	0	7	Restart (2nd order)
9	4	25 / 0	0.85	200		10	0	10	Initial (1st order)
				+200	0.7	10	0	10	Restart (2nd order)
10	4	30 / 0	0.85	200		10	0	10	Initial (1st order)
				+200	0.6	10	0	10	Restart (2nd order)
11	9	25 / 2	0.4	500	1.5	10	100	30	
12	9	25 / 4	0.4	500	1.2	10	100	30	
13	9	25 / 7	0.4	400	1.4	10	200	30	
14	10	25 / 2	0.85	200		5	100	15	Initial (1st order)
				+200	0.8	15	0	15	Restart (2nd order)
15	10	25 / 4	0.85	300		5	100	15	Initial (1st order)
				+300	0.9	15	0	15	Restart (2nd order)
16	10	25 / 7	0.85	300		5	100	15	Initial (1st order)
				+300	0.9	15	0	15	Restart (2nd order)
17	3	12.5 / 0	0.4	400	3.5	15	150	45	
18	3	17.5 / 0	0.4	400	1.4	15	150	45	
19	4	12.5 / 0	0.85	100	1.6	5	50	10	Initial (1st order)
				+300	1.6	10	100	15	Restart (2nd order)
20	4	17.5 / 0	0.85	100		5	50	10	Initial (1st order)
				+300	0.95	10	100	15	Restart (2nd order)

Table 4. Centerline Tail Model USM3D Analysis

Run	Case	α/β	M	Cycles	Residual Reduction	cfl1	iramp	cfl2	Comments
1	1	10 / 0	0.4	400	5.7	75	200	75	
2	1	15 / 0	0.4	300	4.3	75	0	75	
3	1	20 / 0	0.4	300	4.1	75	0	75	
4	1	25 / 0	0.4	300	3.3	75	0	75	
5	1	30 / 0	0.4	400	0.6	10	200	30	
6	2	10 / 0	0.85	400	3.1	20	50	30	
7	2	15 / 0	0.85	400	3.9	20	50	50	
8	2	20 / 0	0.85	400	2.7	10	200	30	
9	2	25 / 0	0.85	400	3.1	10	200	30	
10	2	30 / 0	0.85	400	1.7	10	200	30	
11	6	25 / 2	0.4	400	1.1	15	200	35	
12	6	25 / 4	0.4	400	1.1	15	200	35	
13	6	25 / 7	0.4	400	1.1	15	200	35	
14	8	25 / 2	0.85	400	2.2	10	200	30	
15	8	25 / 4	0.85	200		5	100	15	Initial (1st order)
				+300	0.9	15	0	15	Restart (2nd order)
16	8	25 / 7	0.85						
17	5	15 / 2	0.4	400	4.2	35	0	35	
18	5	15 / 4	0.4	400	3.9	35	0	35	
19	5	15 / 7	0.4	400	2.2	35	0	35	
20	7	15 / 2	0.85	250		10	100	30	Initial
				+150	3.3	30	0	30	Restart
21	7	15 / 4	0.85	250		5	100	30	Initial
				+150	3.2	30	0	30	Restart
22	7	15 / 7	0.85						



Twin Tail Model



Centerline Tail Model

Geometric parameters (Full configuration; all dimensions in inches)

Area (S_{ref})	208.19
Chord (c_{ref})	12.968
Span (b)	19.2
Moment Center (from nose)	(20.355, 0, 0)
Chine angle (included)	30°
Wing leading-edge sweep	60°

Figure 1. Geometric features of modular transonic vortex interaction (MTVI) models

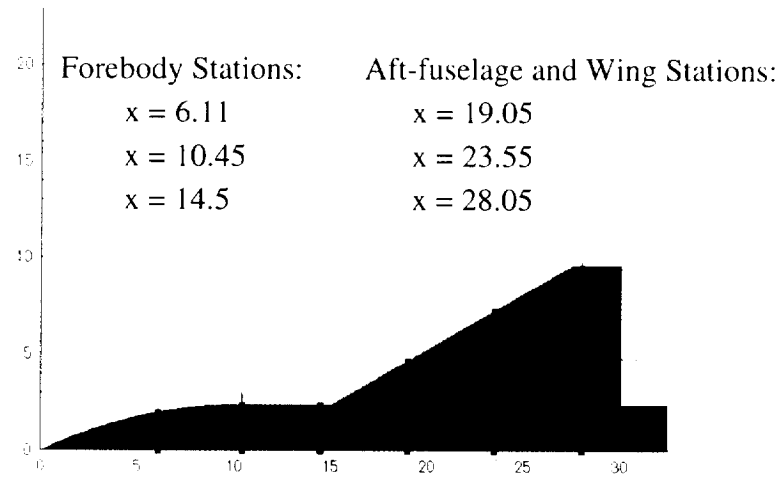


Figure 2. Cross-flow stations for surface C_p correlations

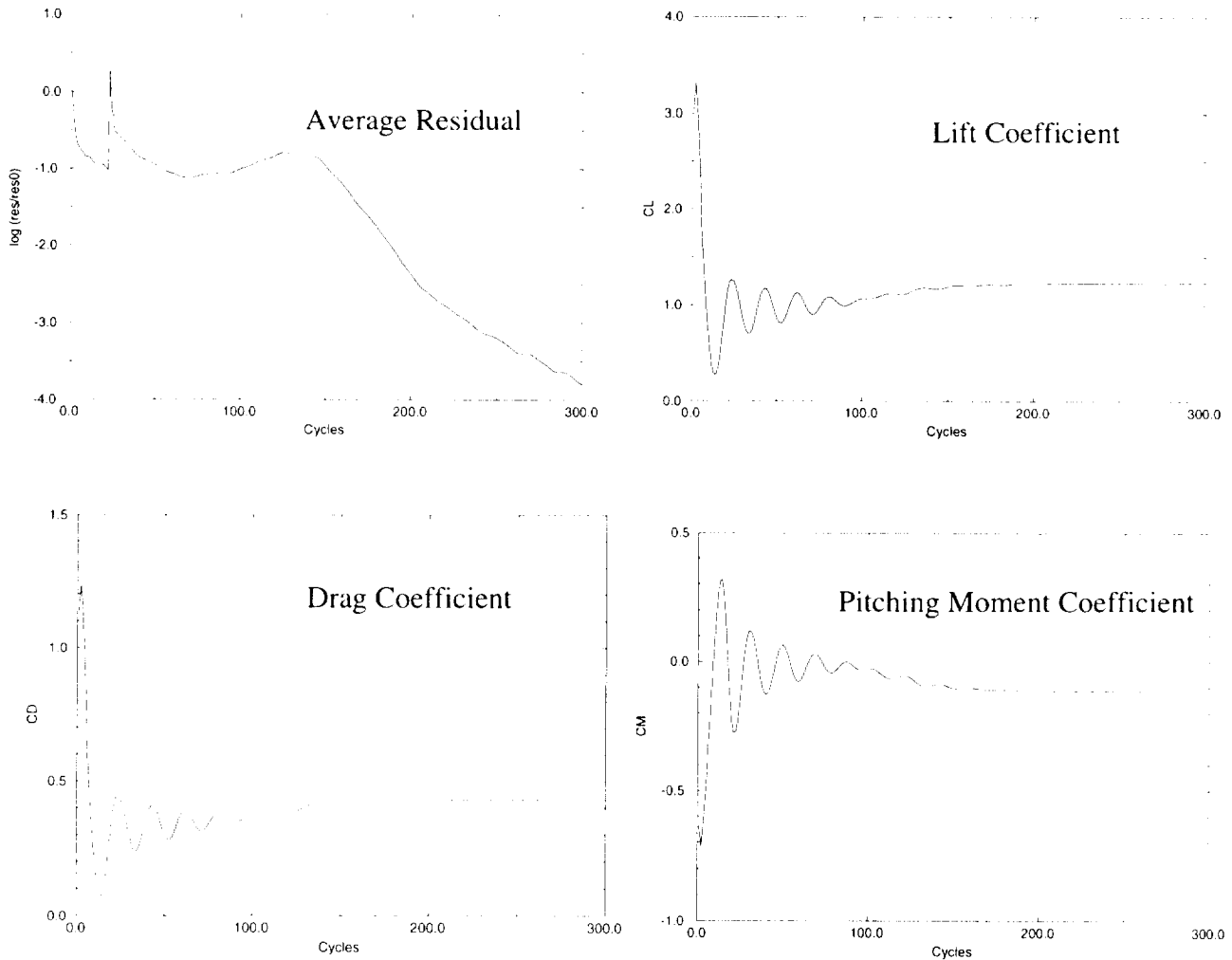


Figure 3. Convergence histories of USM3D analysis of MTVI Centerline Tail model, Grid 4 (see Table 2), $M = 0.4$, $\alpha = 20^\circ$

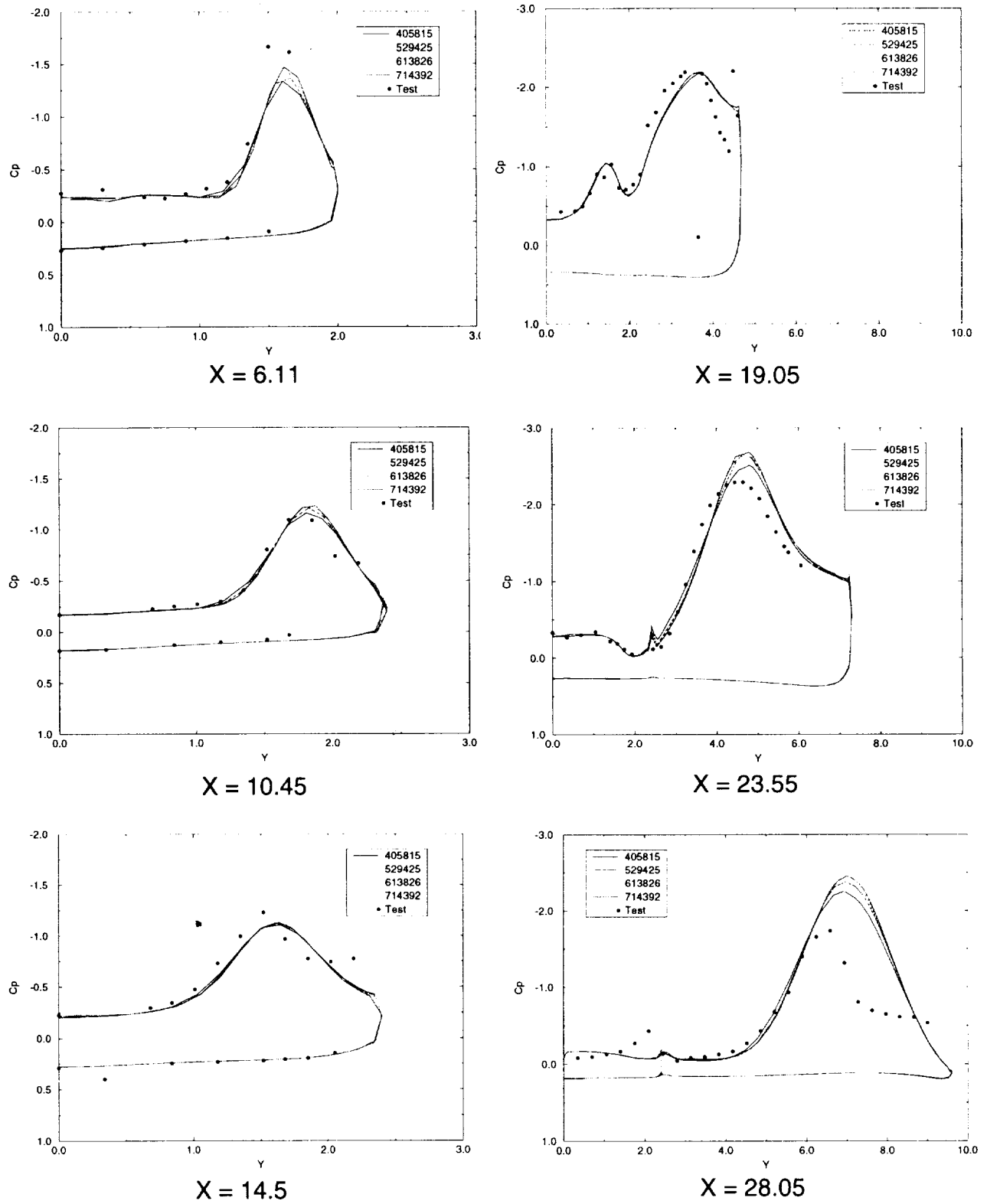


Figure 4. Grid sensitivity of surface C_p in USM3D analysis of MTVI Centerline Tail model, $M = 0.4$, $\alpha = 20^\circ$

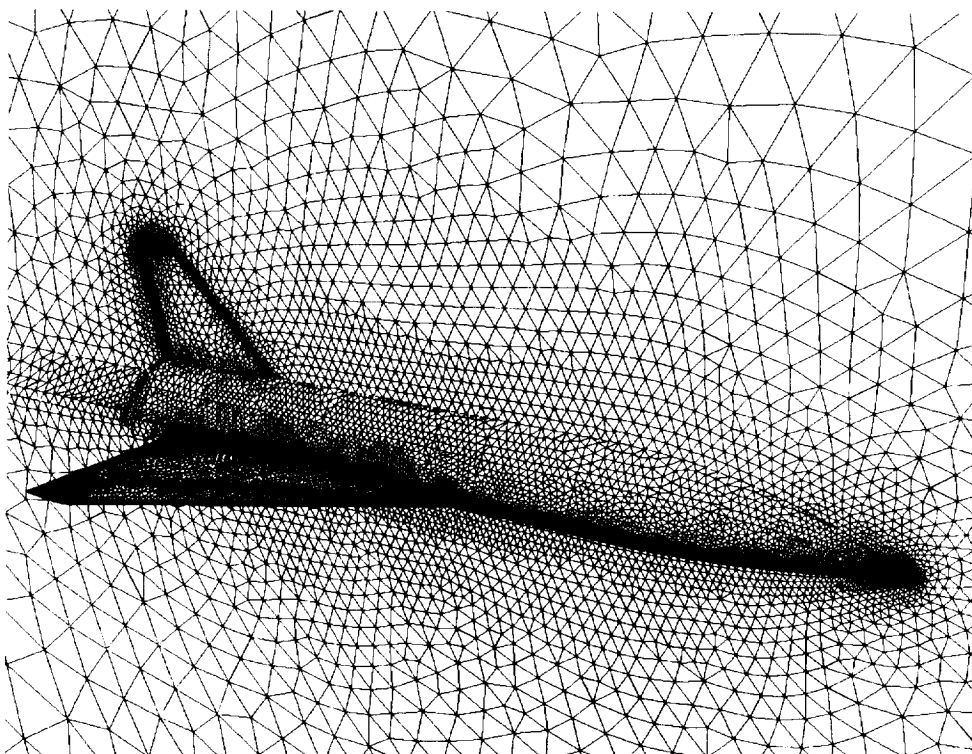


Figure 5. Perspective view of surface and plane-of-symmetry grid on MTVI Centerline Tail model with 613,826 cells (Grid 3).

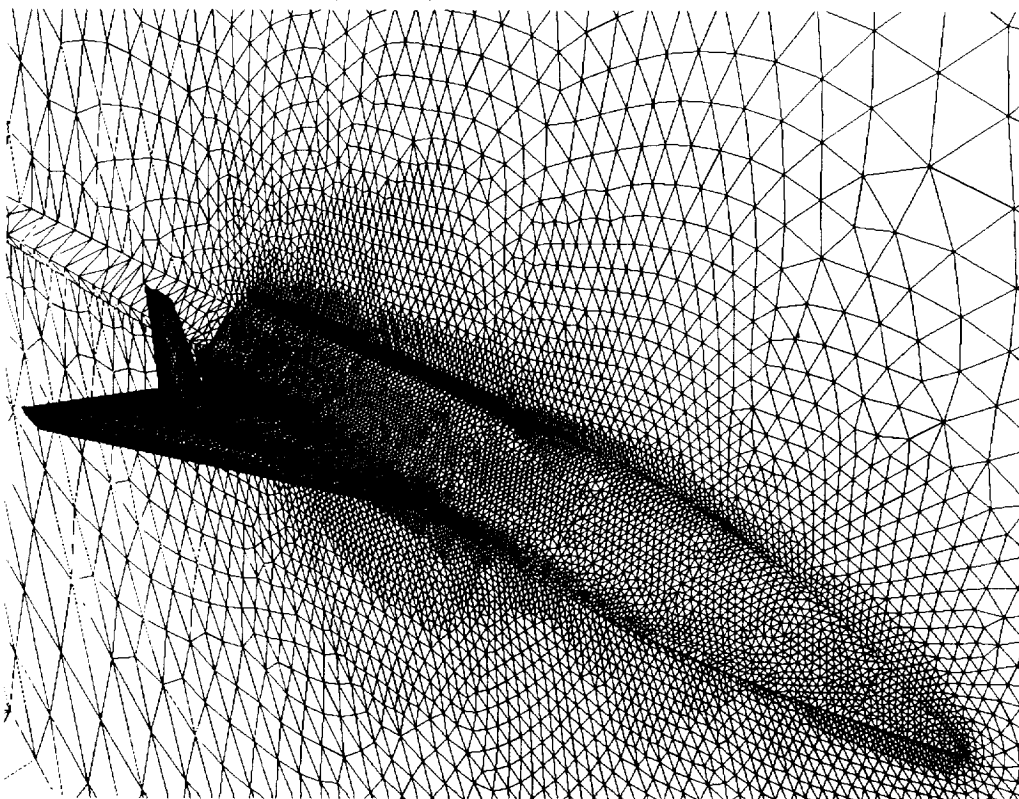


Figure 6. Perspective view of surface and plane-of-symmetry grid on MTVI Twin Tail model with 821,826 cells.

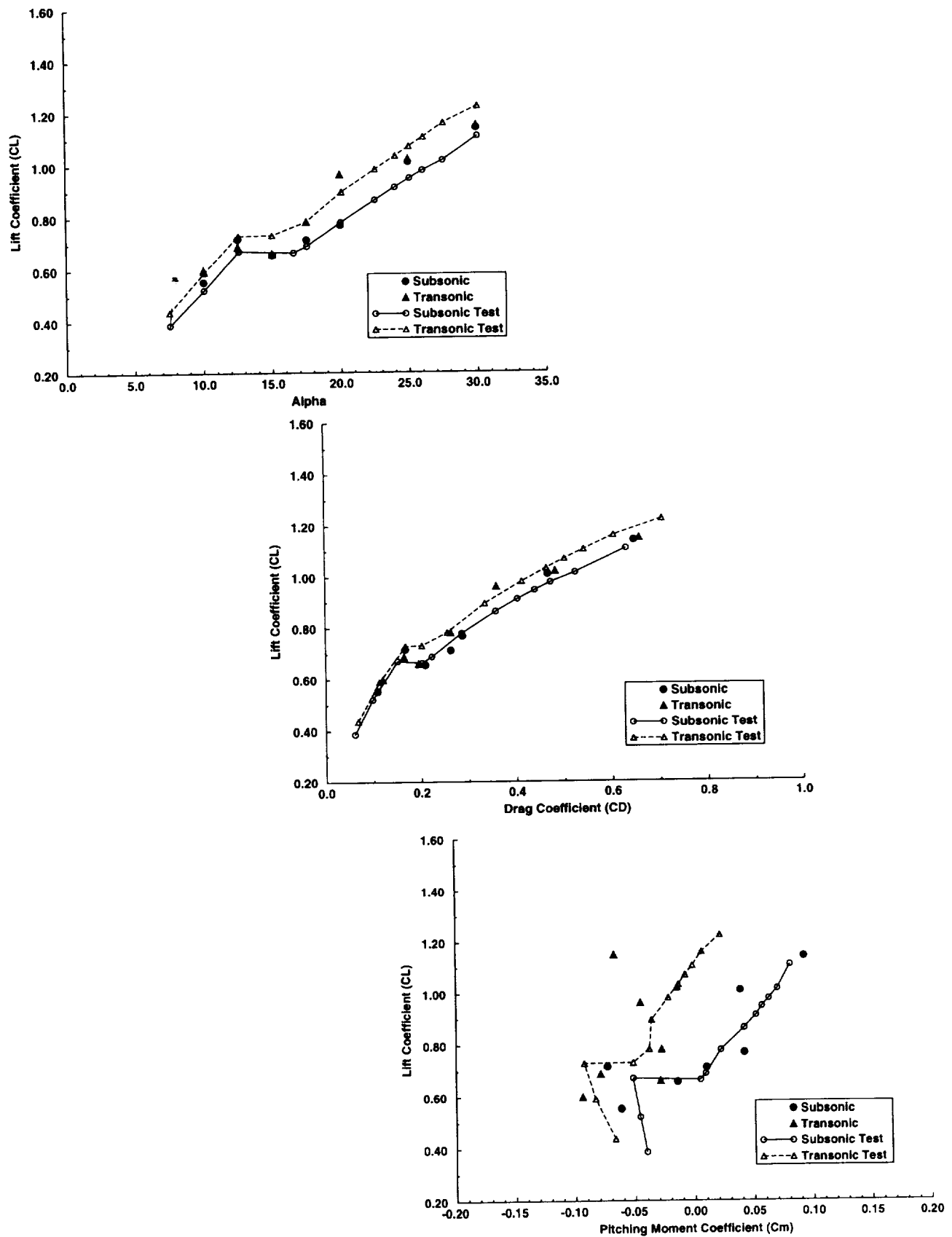


Figure 7. Compressibility effects for force and moment coefficients on twin tail model in subsonic ($M = 0.4$) and transonic ($M = 0.85$) conditions

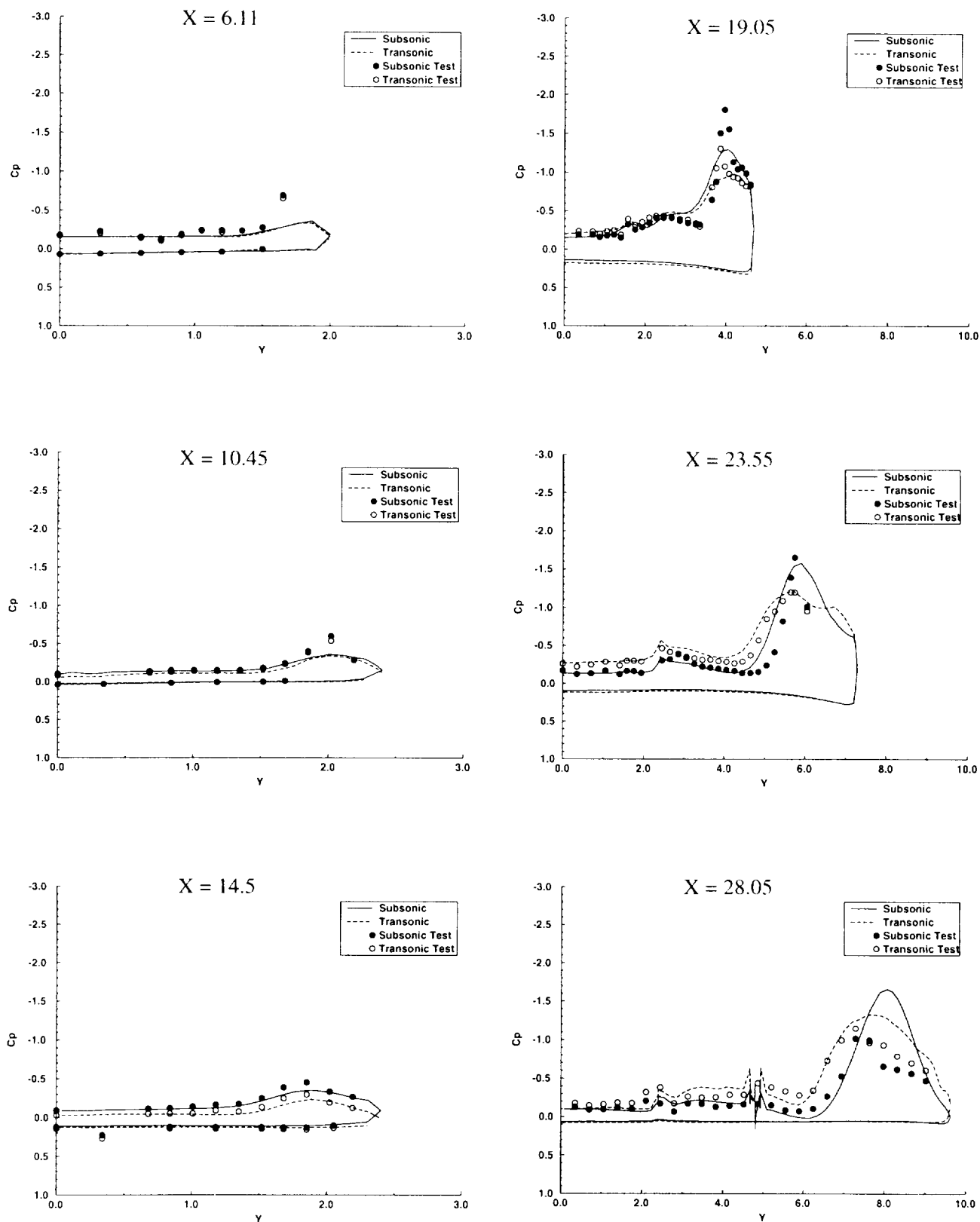


Figure 8. Compressibility effects on surface pressure distributions for twin tail model, $\alpha = 10^\circ$, subsonic ($M = 0.4$) and transonic ($M = 0.85$) conditions

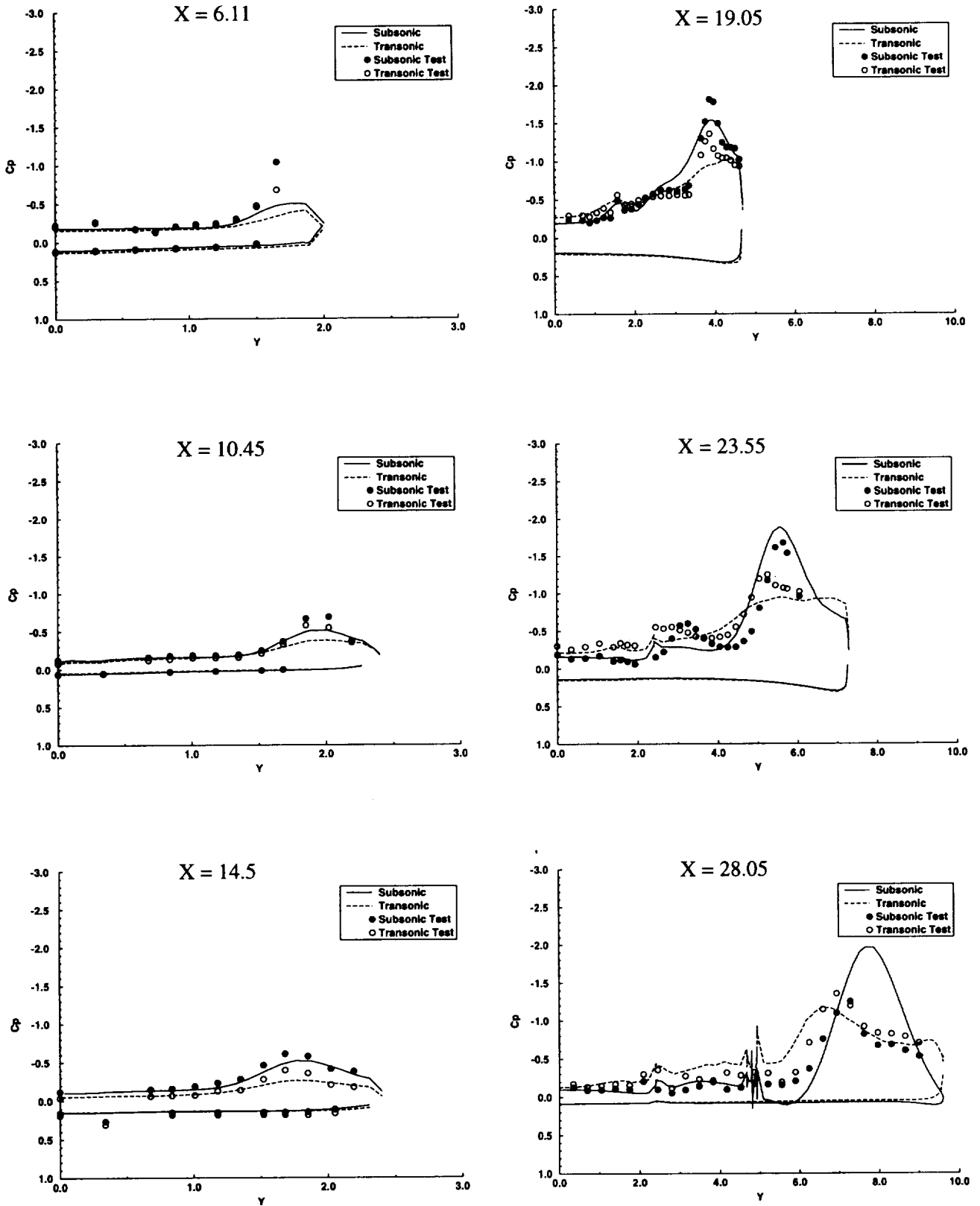


Figure 9. Compressibility effects on surface pressure distributions for twin tail model, $\alpha = 12.5^\circ$, subsonic ($M = 0.4$) and transonic ($M = 0.85$) conditions

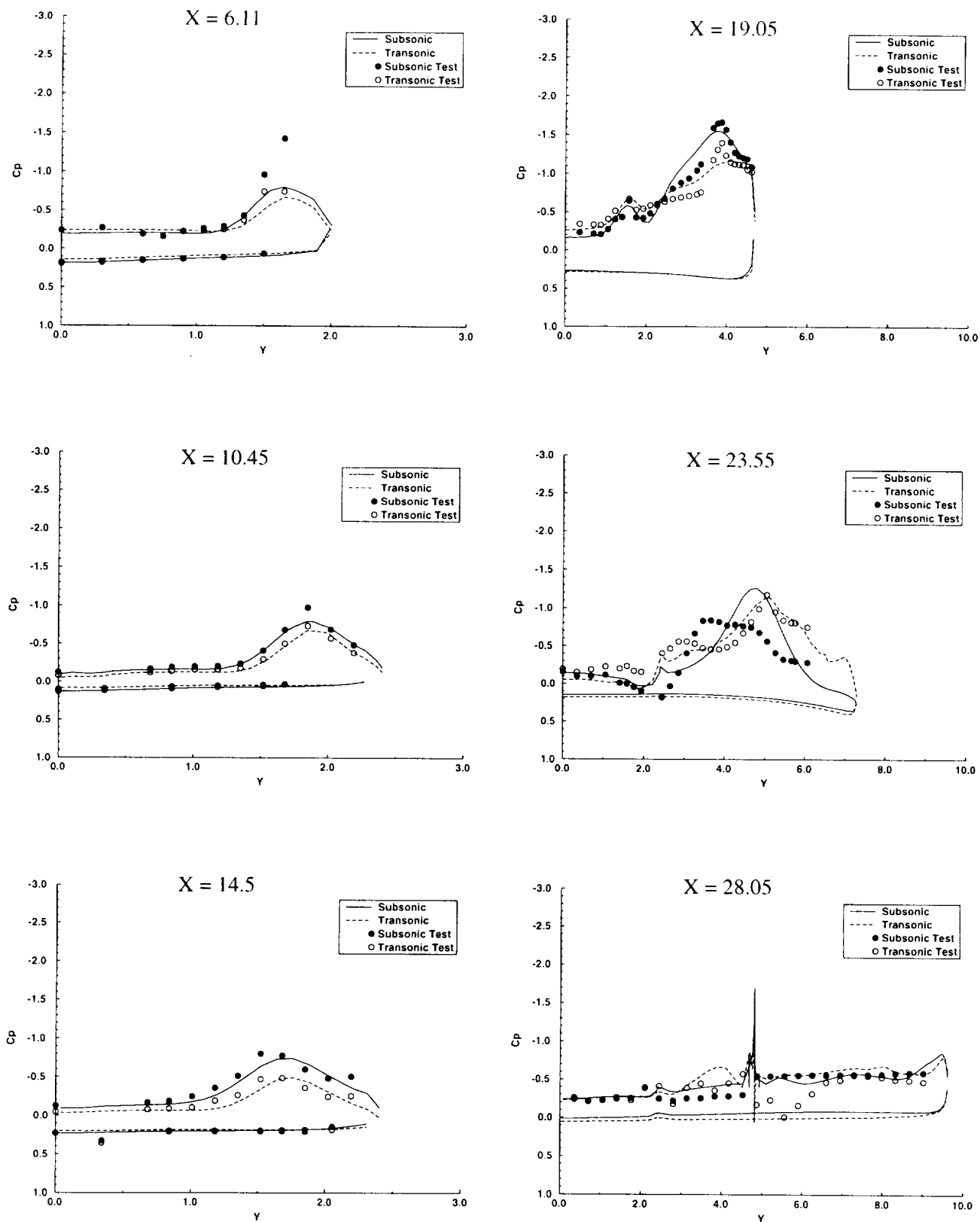


Figure 10. Compressibility effects on surface pressure distributions for twin tail model, $\alpha = 15^\circ$, subsonic ($M = 0.4$) and transonic ($M = 0.85$) conditions

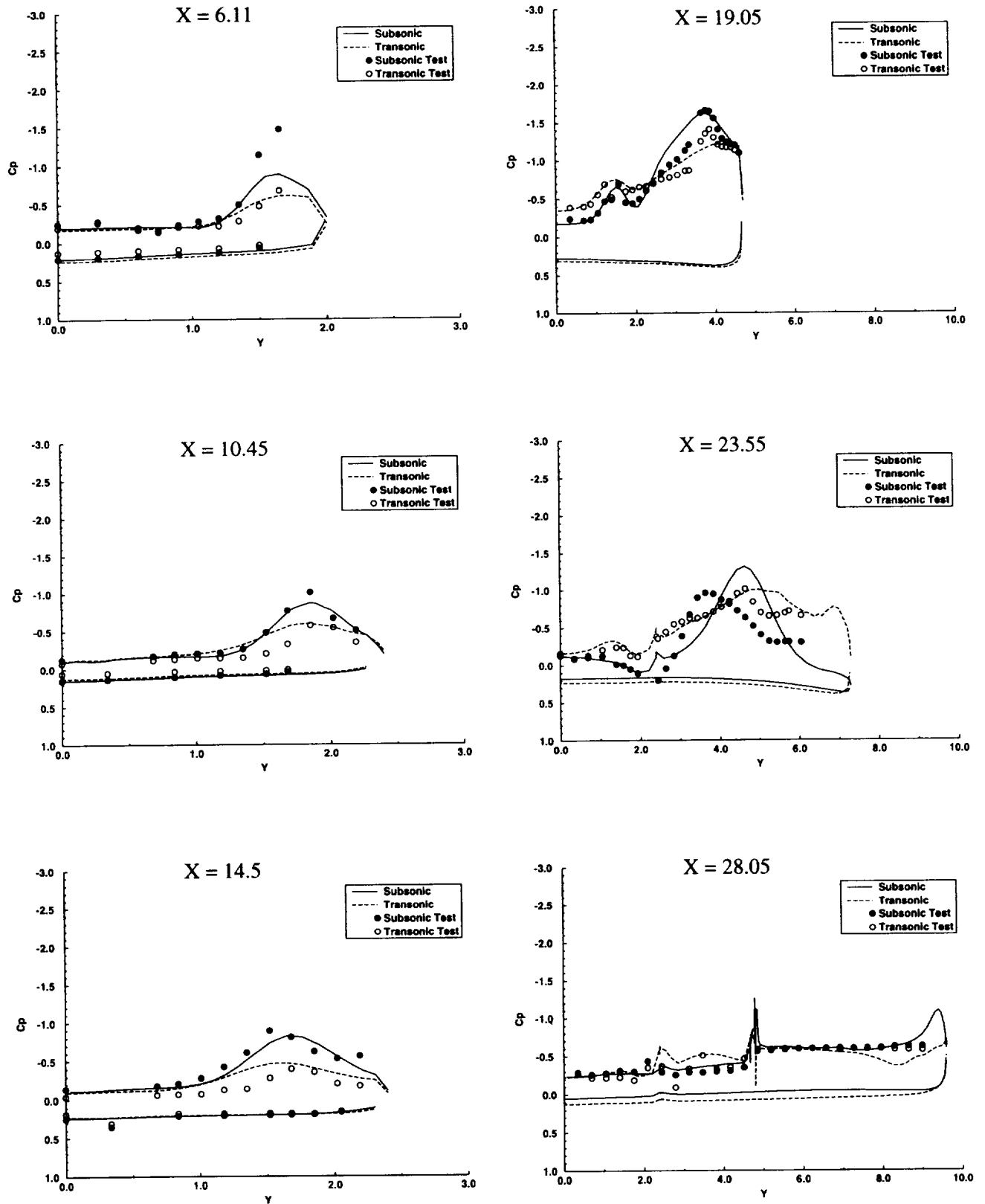


Figure 11. Compressibility effects on surface pressure distributions for twin tail model, $\alpha = 17.5^\circ$, subsonic ($M = 0.4$) and transonic ($M = 0.85$) conditions

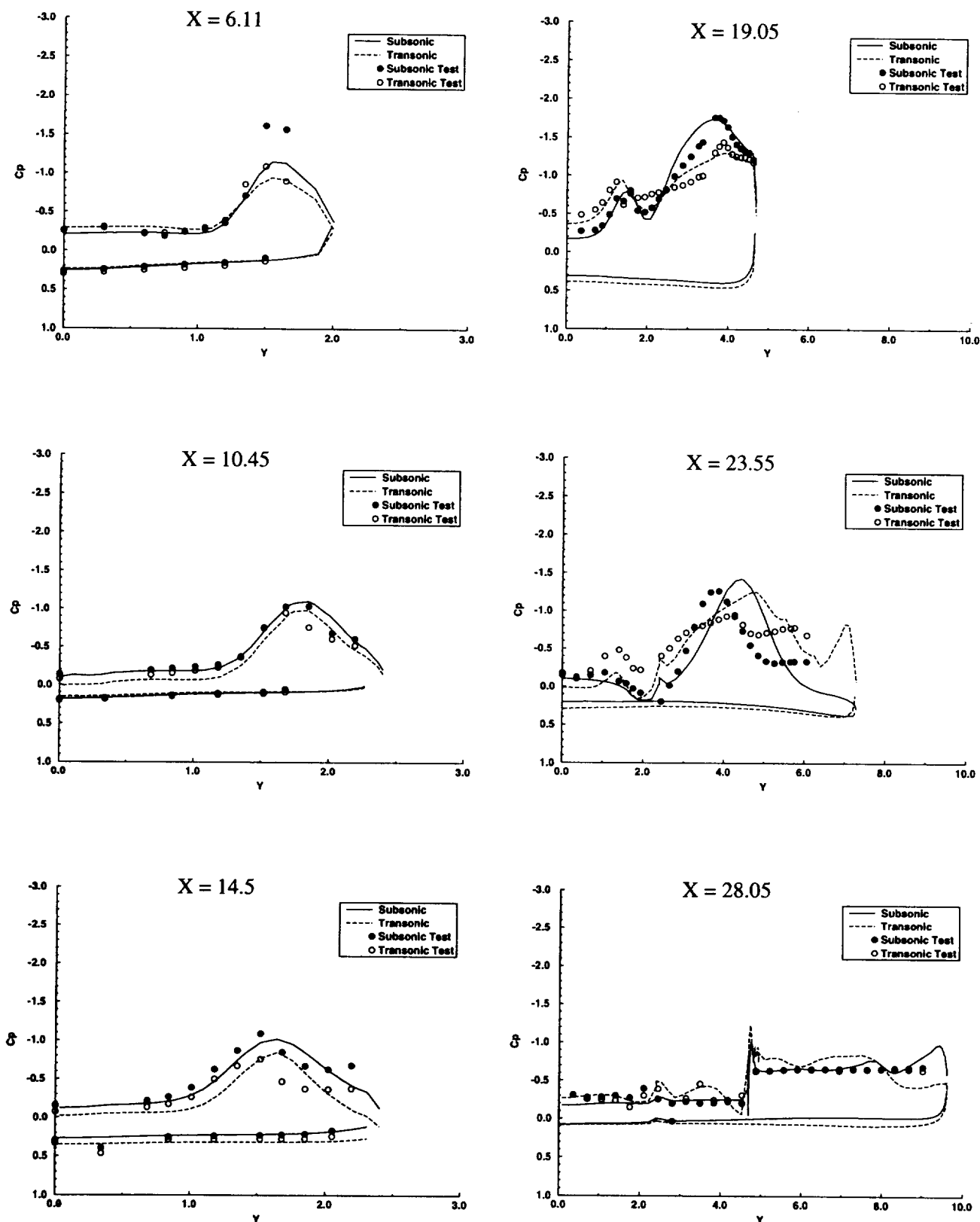


Figure 12. Compressibility effects on surface pressure distributions for twin tail model, $\alpha = 20^\circ$, subsonic ($M = 0.4$) and transonic ($M = 0.85$) conditions

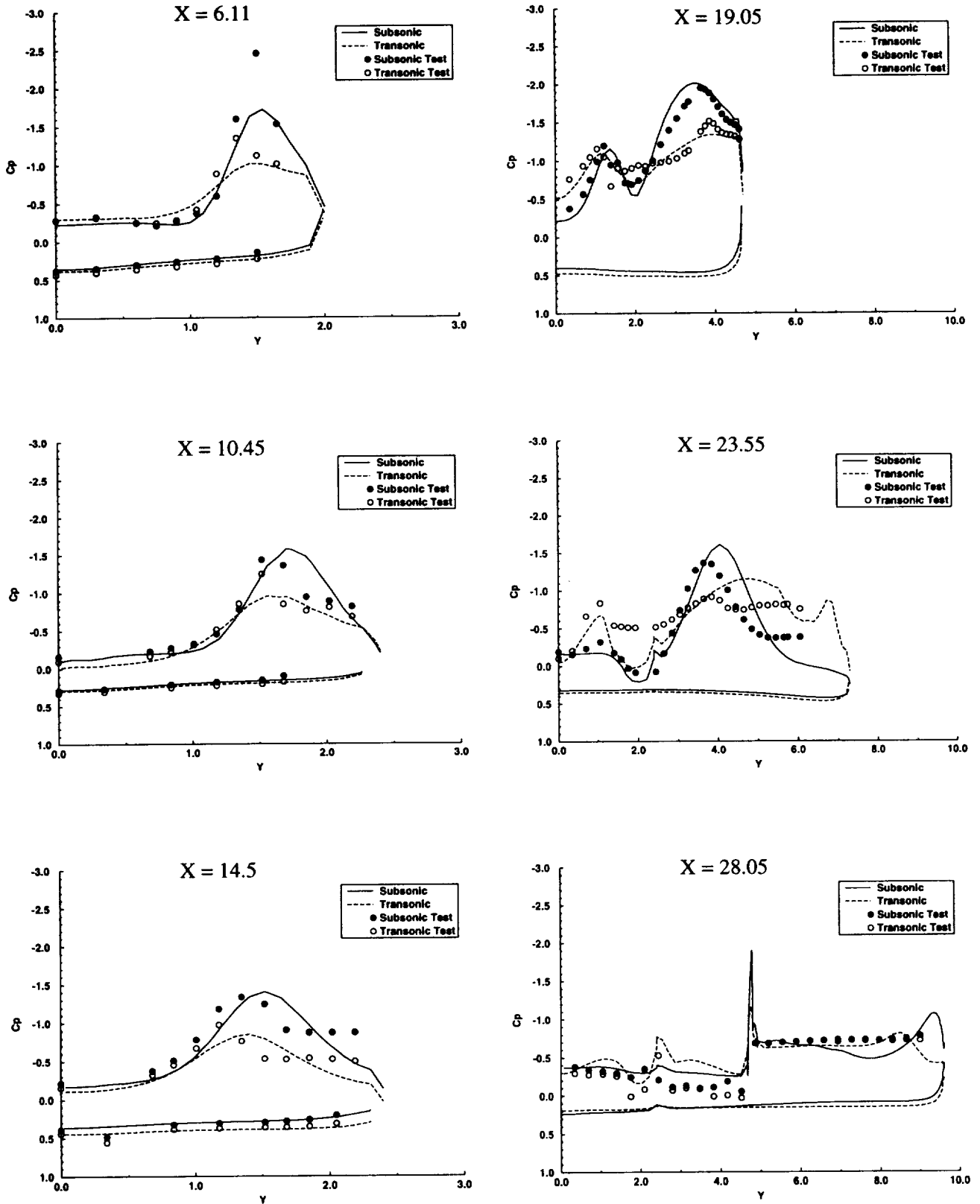


Figure 13. Compressibility effects on surface pressure distributions for twin tail model, $\alpha = 25^\circ$, subsonic ($M = 0.4$) and transonic ($M = 0.85$) conditions

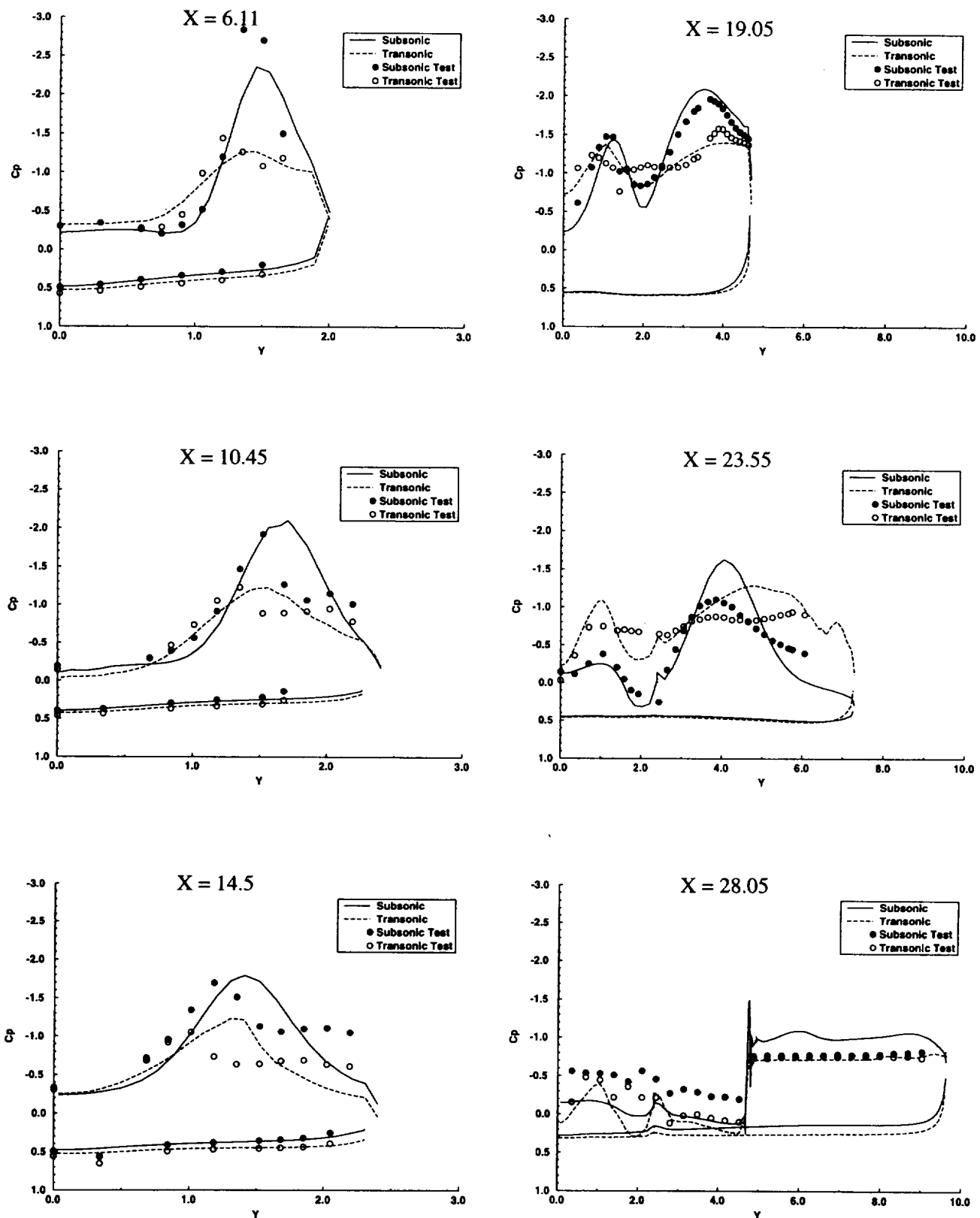


Figure 14. Compressibility effects on surface pressure distributions for twin tail model, $\alpha = 30^\circ$, subsonic ($M = 0.4$) and transonic ($M = 0.85$) conditions

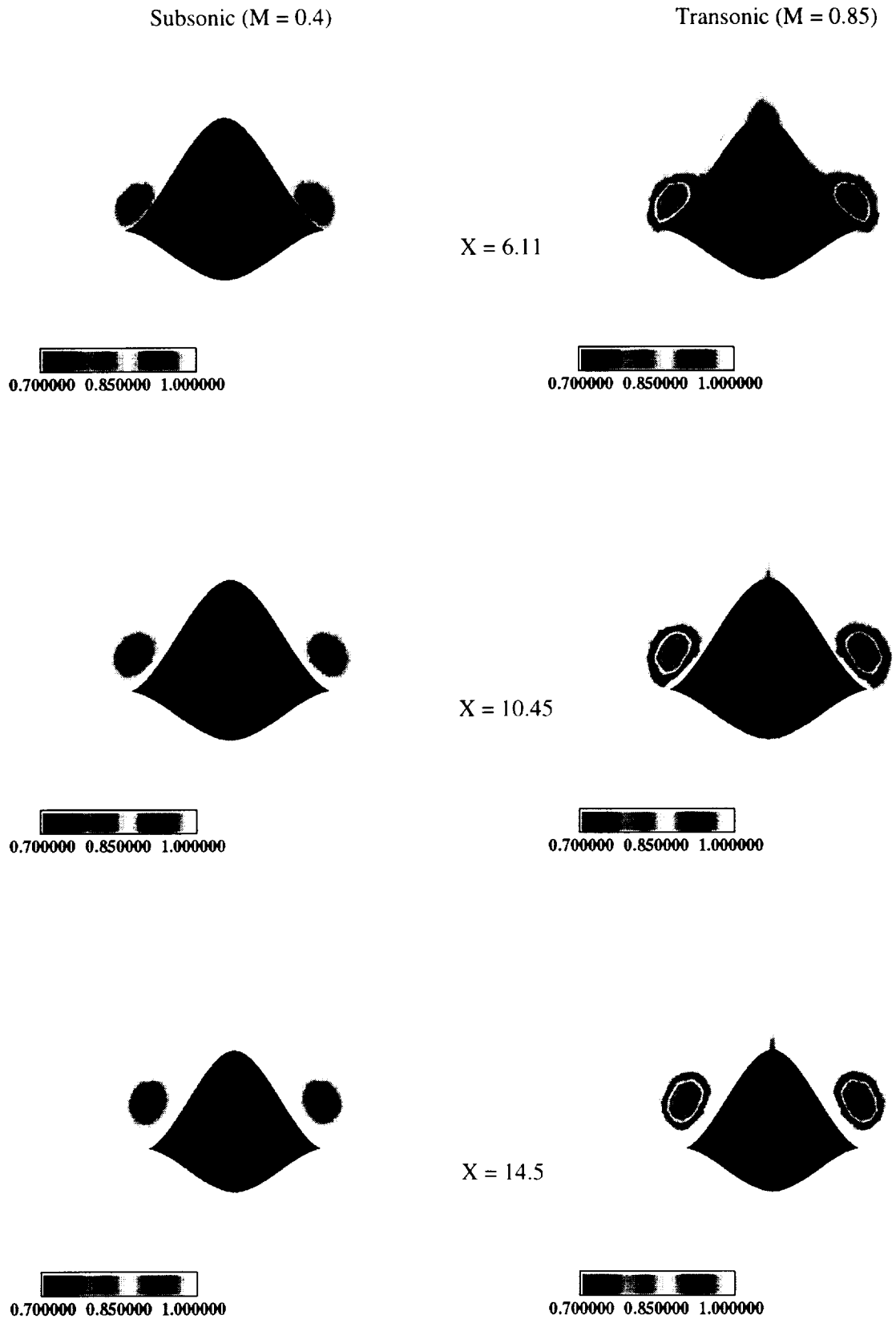
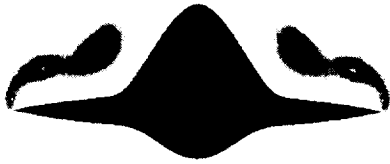


Figure 15. Compressibility effects on off-body total pressure distributions for twin tail configuration, forebody stations, $\alpha = 20^\circ$, subsonic (left column) and transonic (right column) conditions

Subsonic ($M = 0.4$)

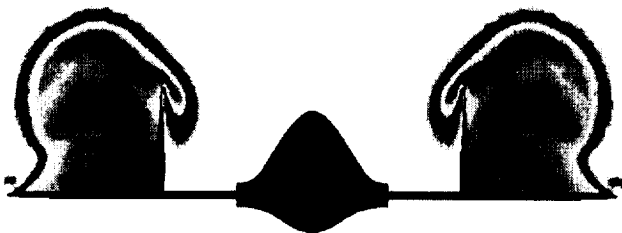
Transonic ($M = 0.85$)



$X = 19.05$



$X = 23.55$



$X = 28.05$

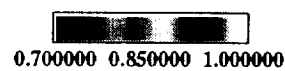
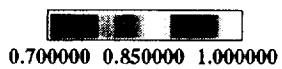
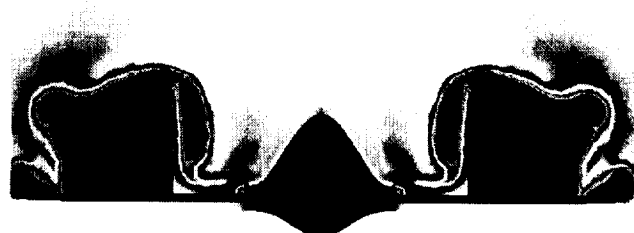


Figure 16. Compressibility effects on off-body total pressure distributions for twin tail model, aftbody-wing stations, $\alpha = 20^\circ$, subsonic (left column) and transonic (right column) conditions

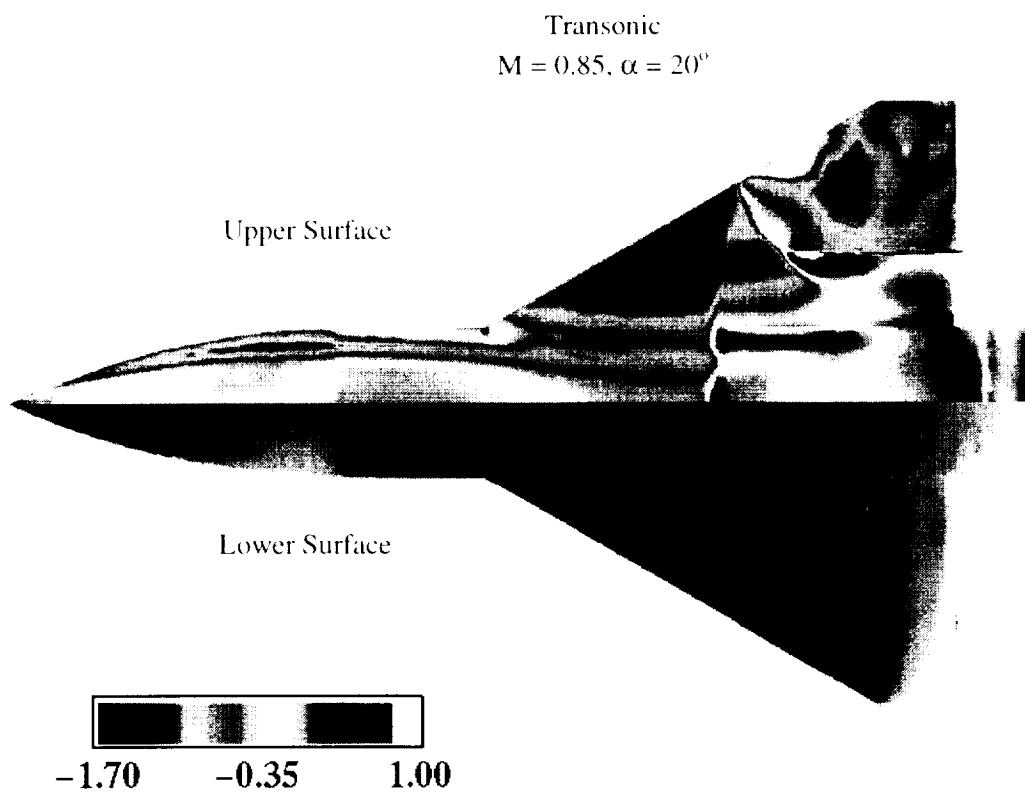
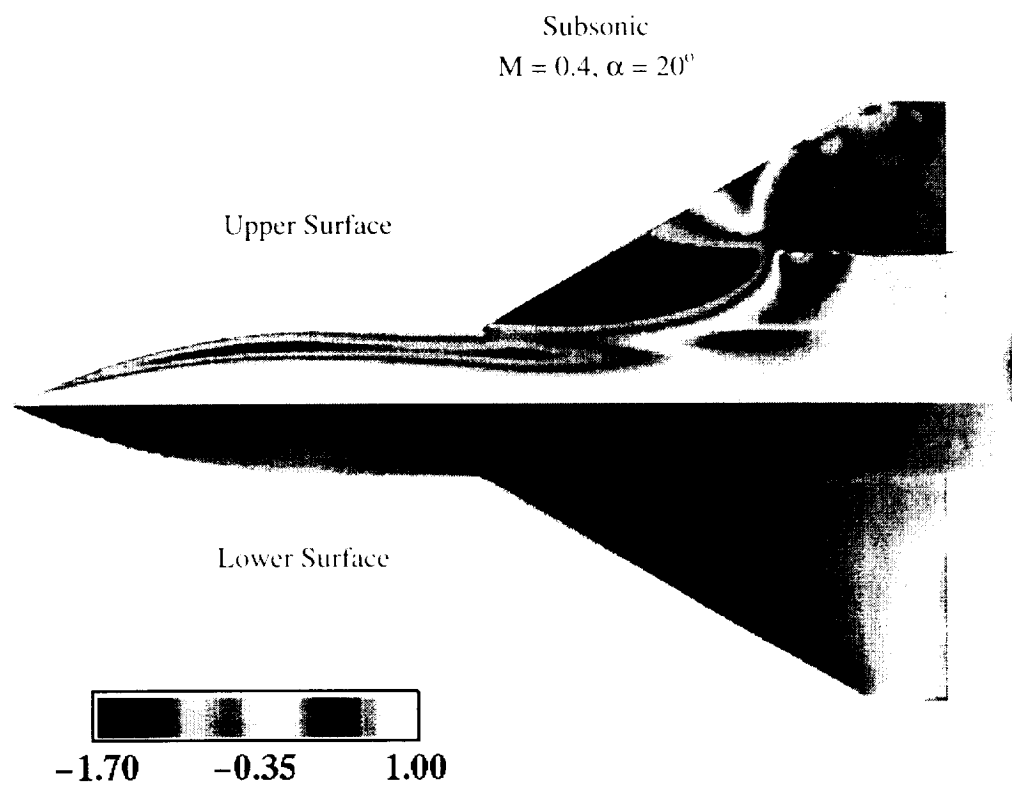


Figure 17. Compressibility effects on surface C_p distributions for twin tail configuration, $\alpha = 20^\circ$

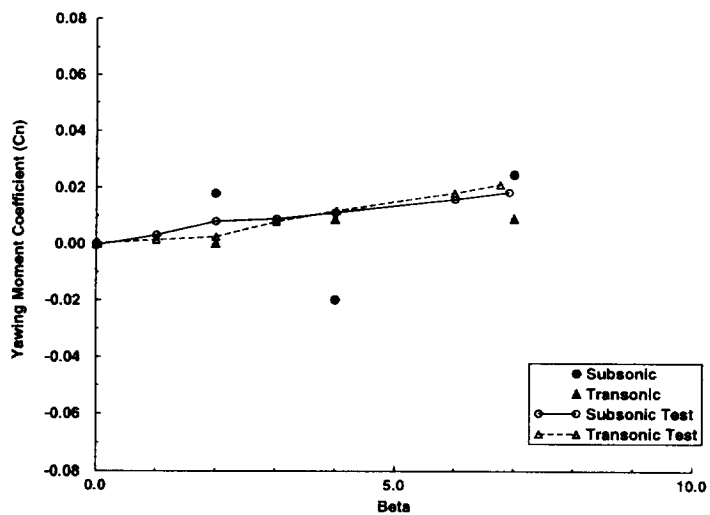
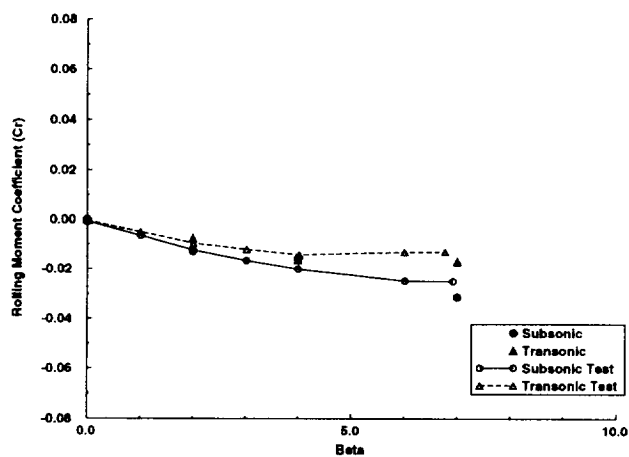
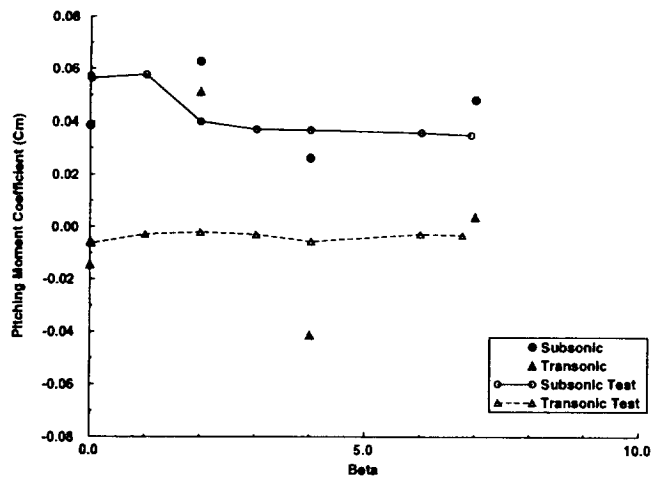


Figure 18. Compressibility effects on moment coefficients in side slip for twin tail model, $\alpha = 25^\circ$, subsonic ($M = 0.4$) and transonic ($M = 0.85$) conditions

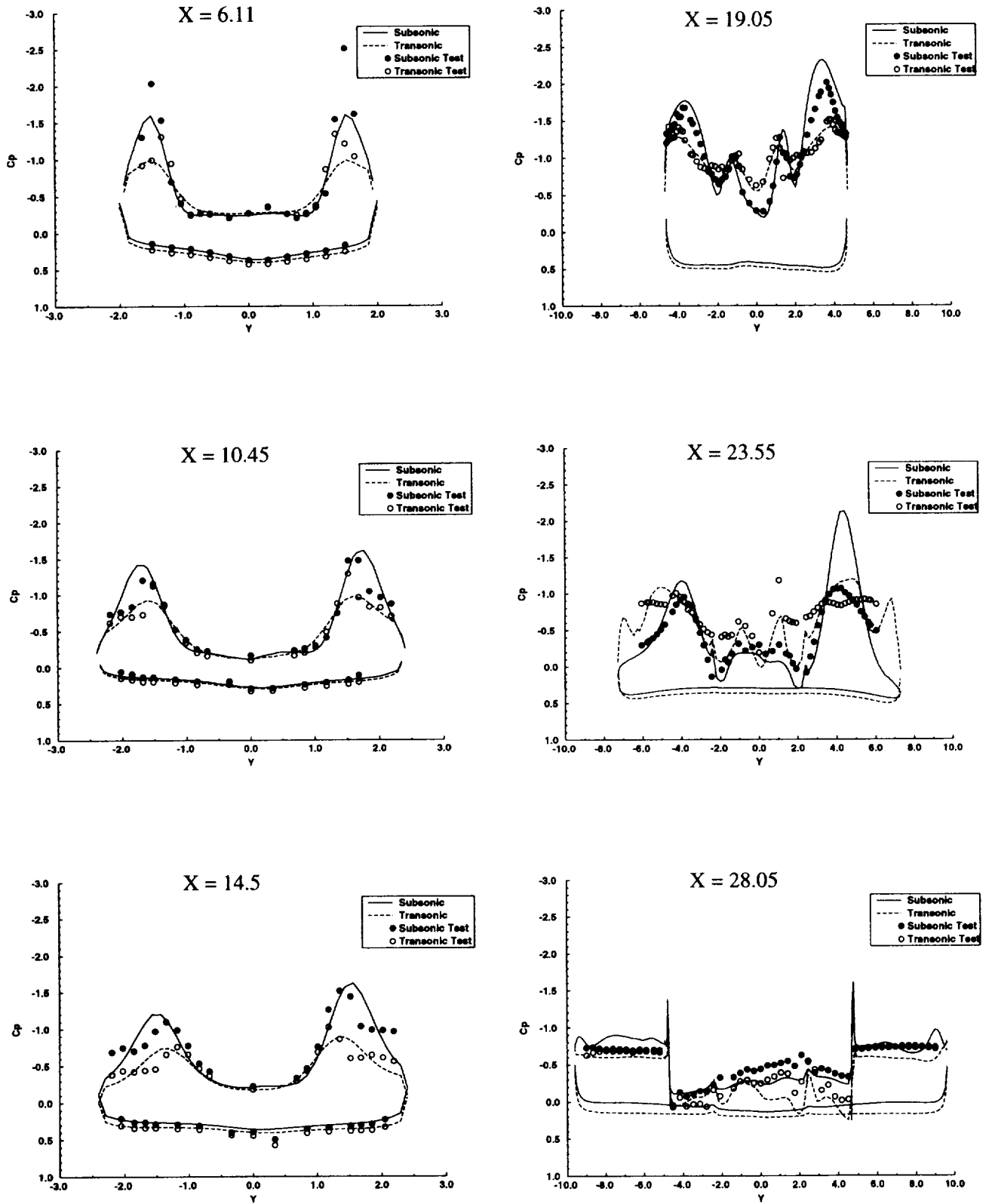


Figure 19. Compressibility effects on surface pressure distributions for twin tail model, $\alpha = 25^\circ$, $\beta = 2^\circ$, subsonic ($M = 0.4$) and transonic ($M = 0.85$) conditions

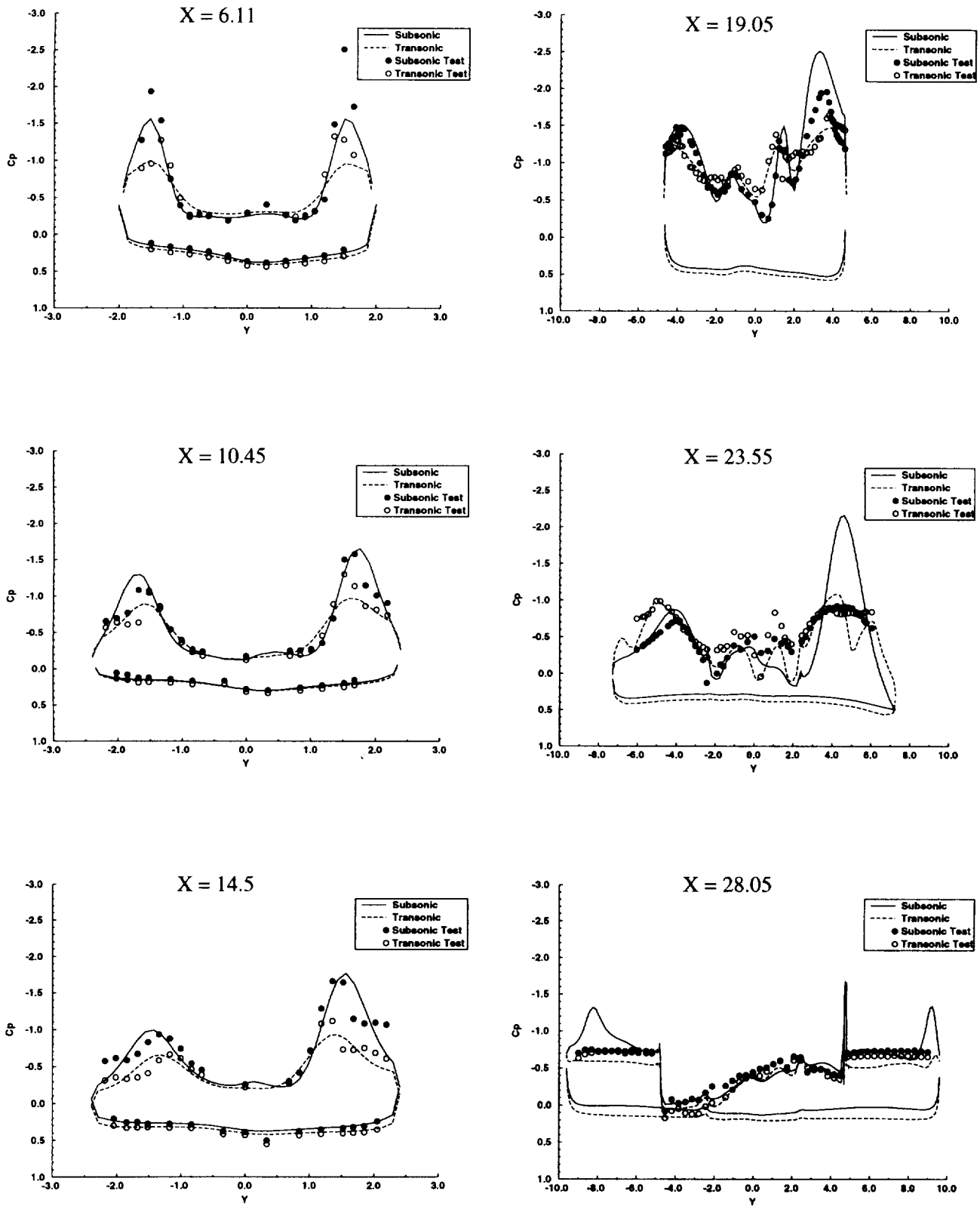


Figure 20. Compressibility effects on surface pressure distributions for twin tail model, $\alpha = 25^\circ$, $\beta = 4^\circ$, subsonic ($M = 0.4$) and transonic ($M = 0.85$) conditions

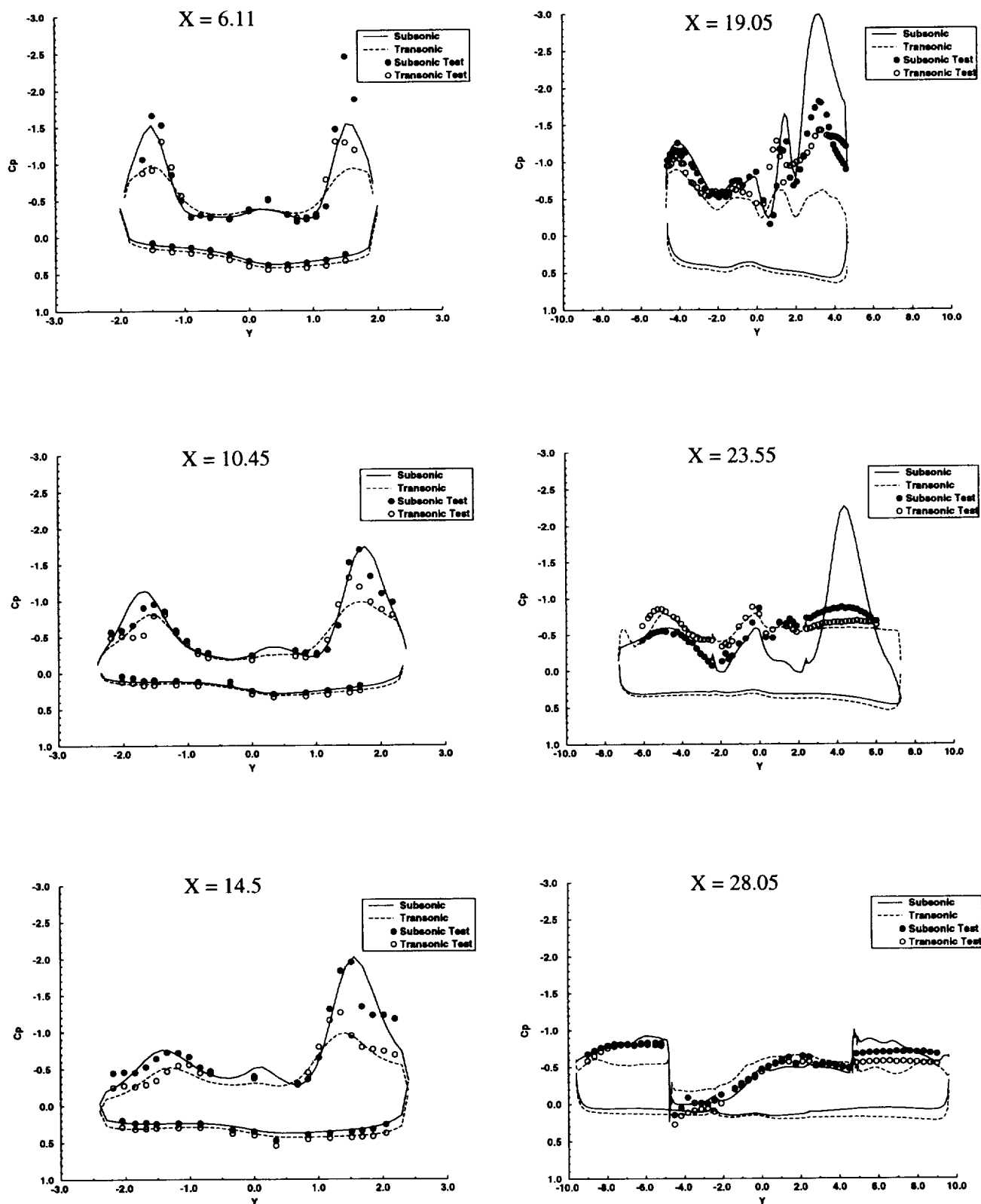


Figure 21. Compressibility effects on surface pressure distributions for twin tail model, $\alpha = 25^\circ$, $\beta = 7^\circ$, subsonic ($M = 0.4$) and transonic ($M = 0.85$) conditions

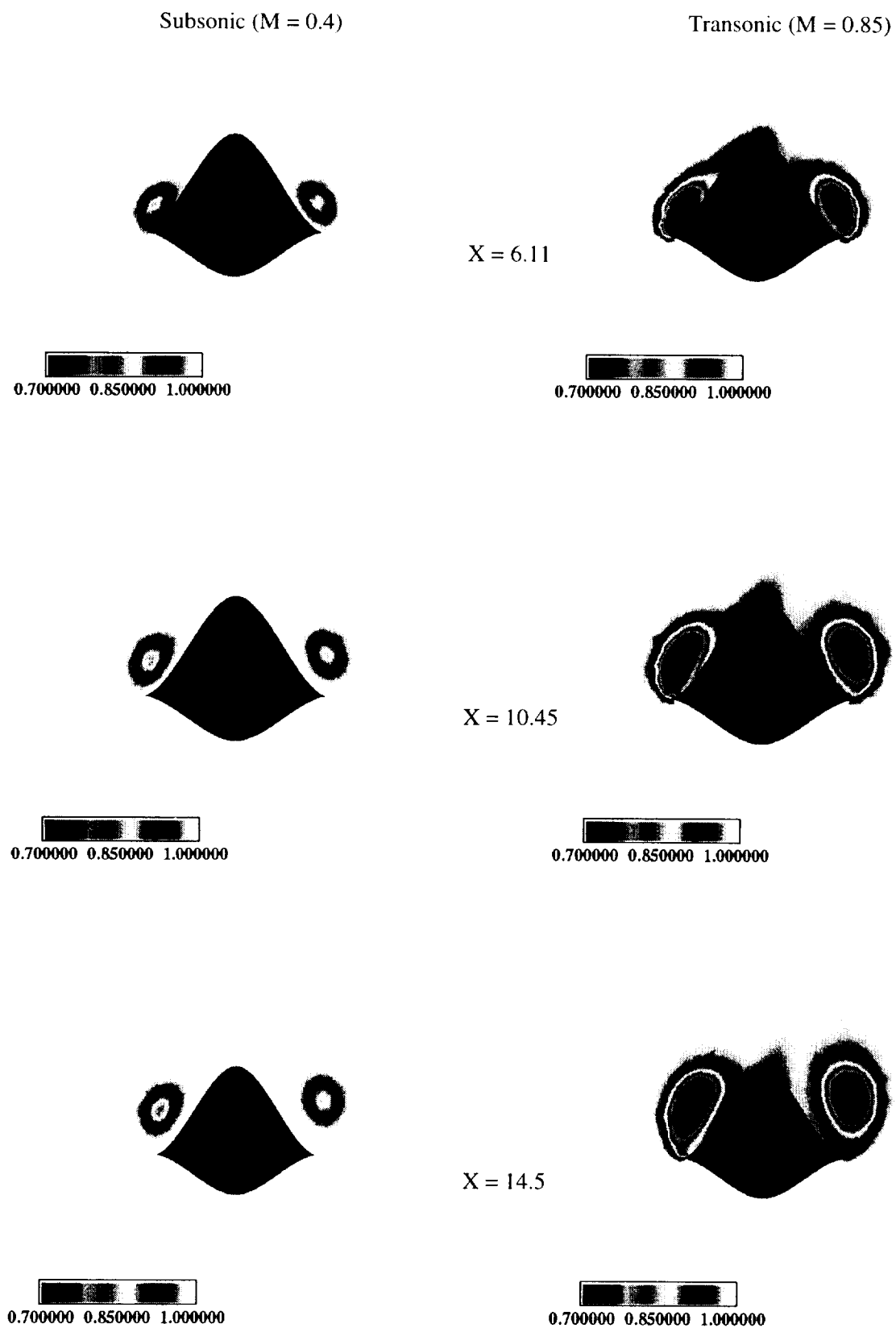


Figure 22. Compressibility effects on off-body total pressure distributions for twin tail configuration, forebody stations, $\alpha = 25^\circ$, $\beta = 4^\circ$, subsonic (left column) and transonic (right column)

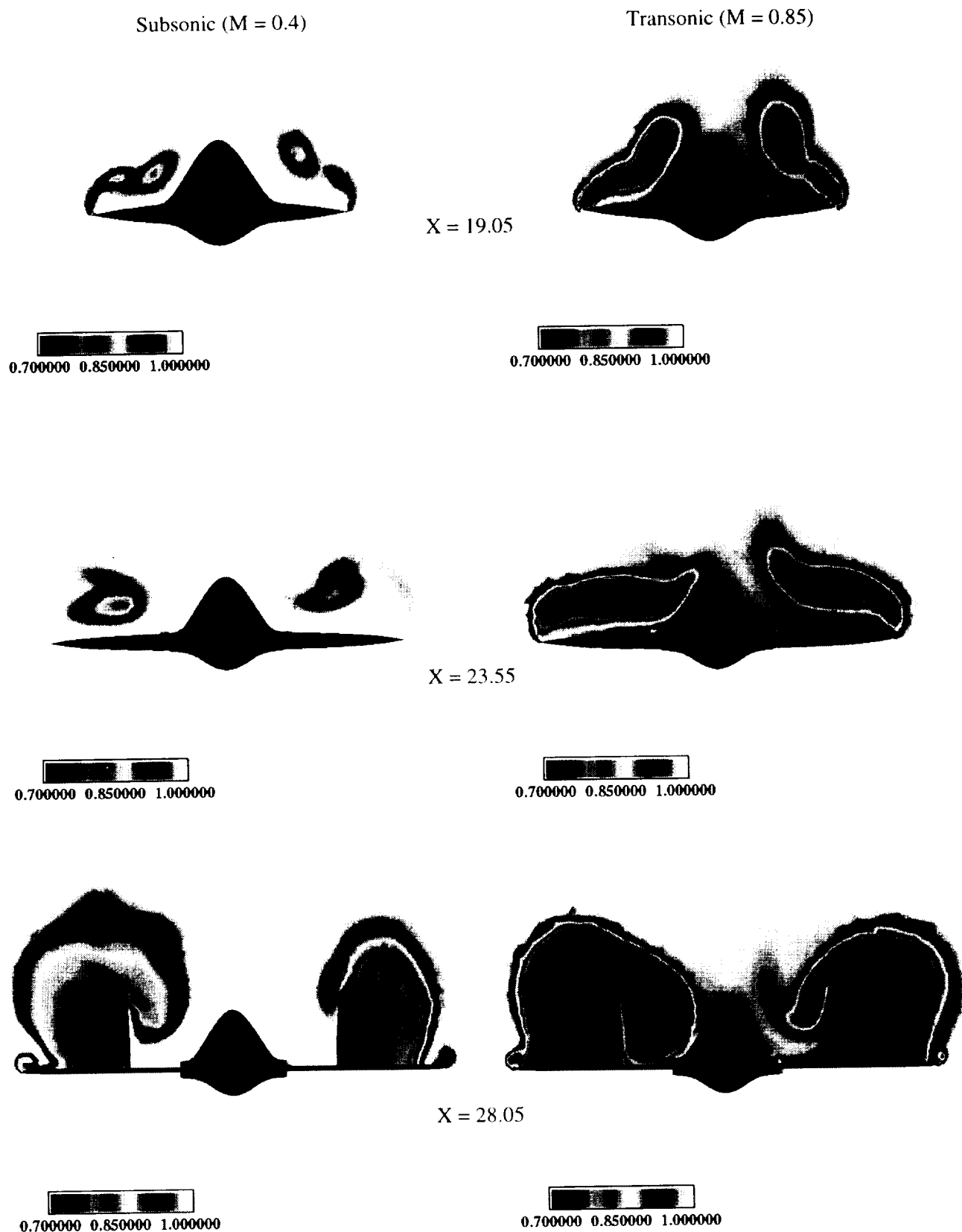
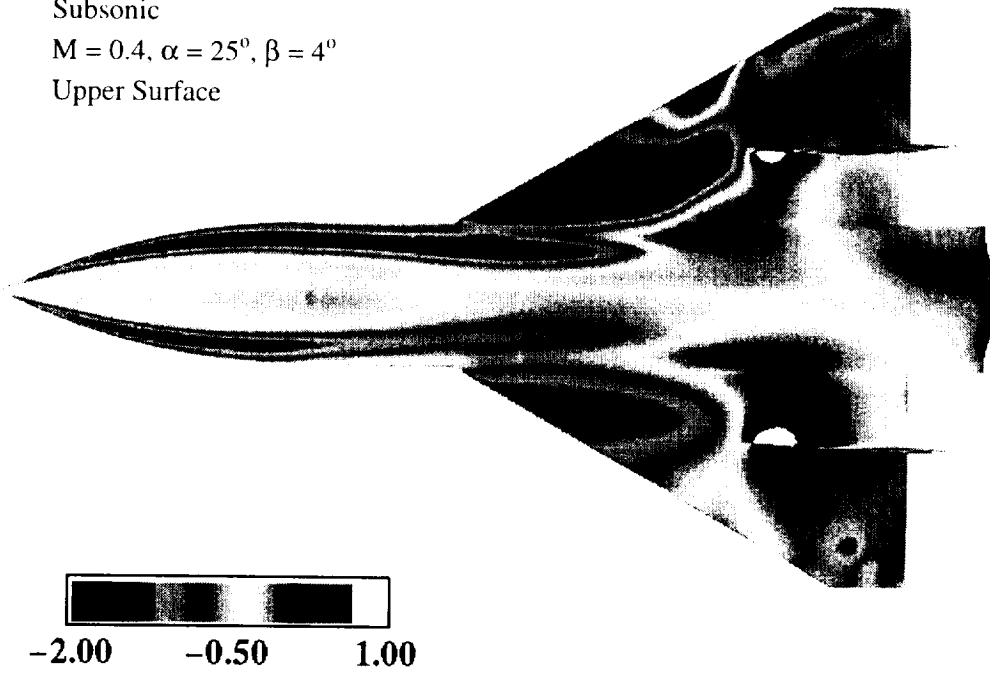


Figure 23. Compressibility effects on off-body total pressure distributions for twin tail configuration, aftbody-wing stations, $\alpha = 25^\circ$, $\beta = 4^\circ$, subsonic (left column) and transonic (right column)

Subsonic

$M = 0.4$, $\alpha = 25^\circ$, $\beta = 4^\circ$

Upper Surface



Transonic

$M = 0.85$, $\alpha = 25^\circ$, $\beta = 4^\circ$

Upper Surface

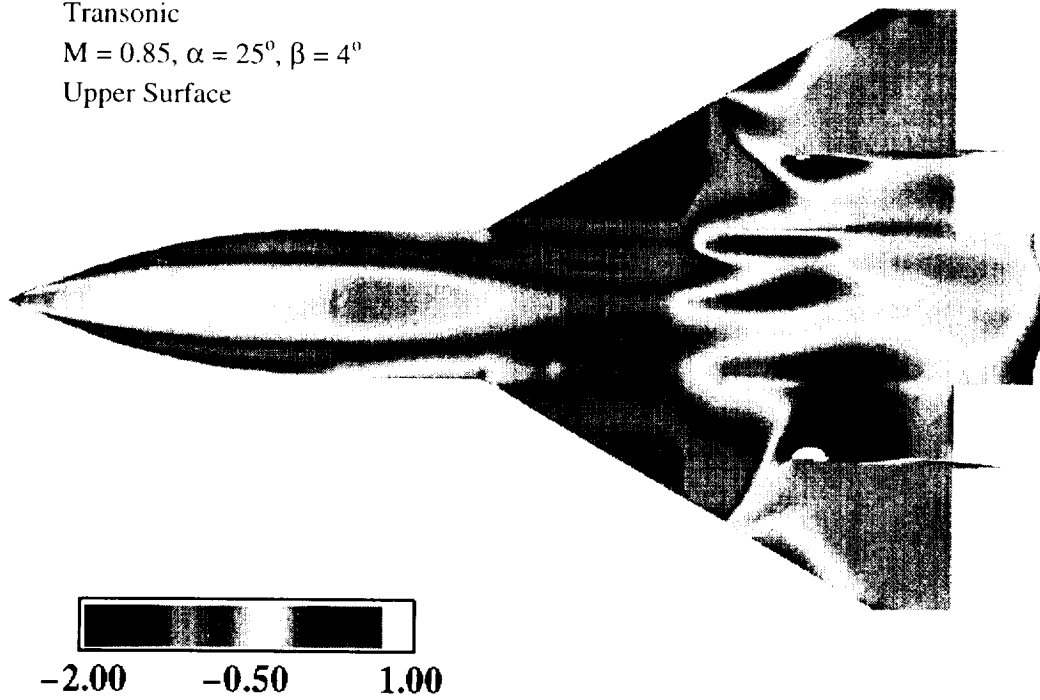


Figure 24. Compressibility effects on surface C_p distributions for twin tail configuration, $\alpha = 25^\circ$, $\beta = 4^\circ$

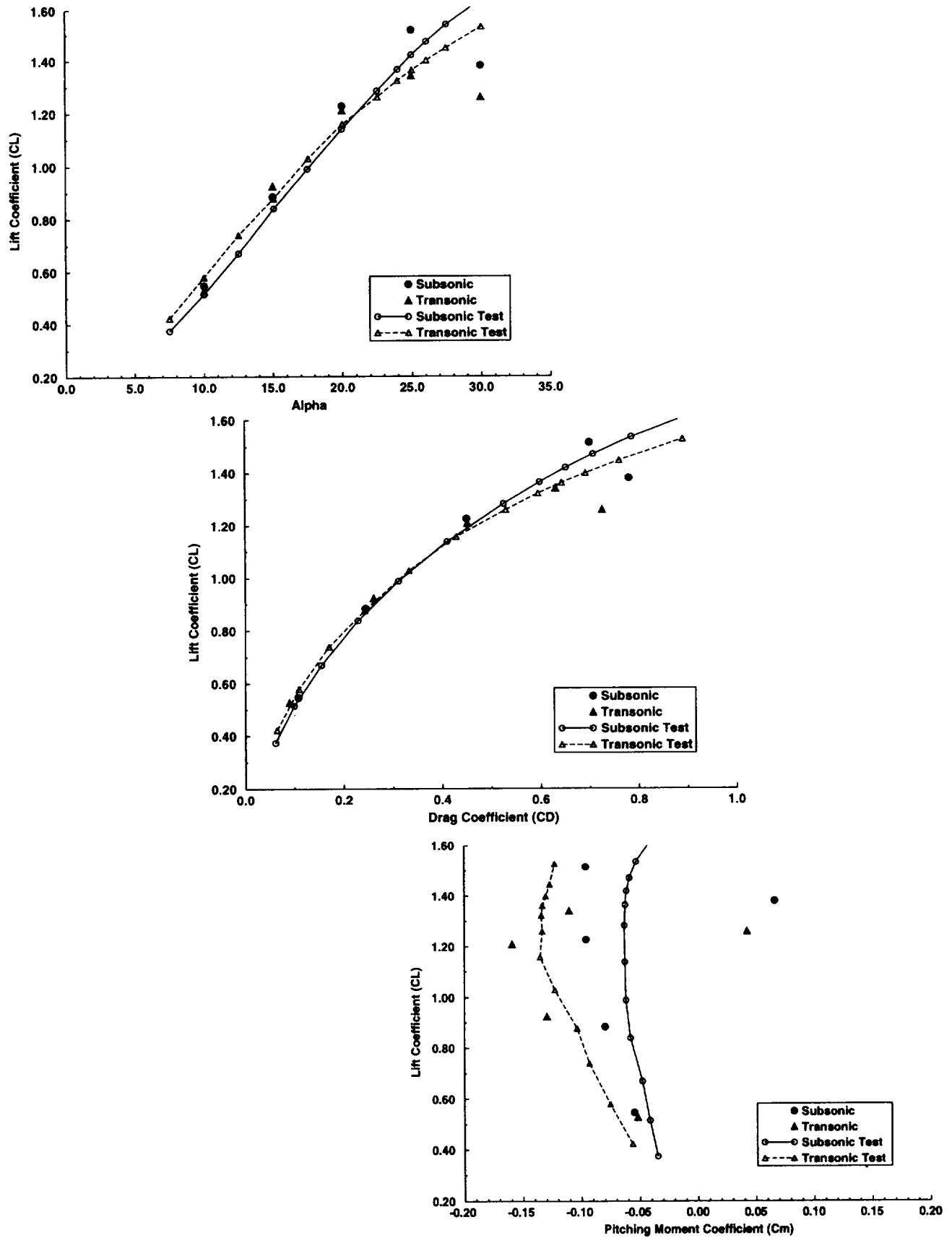


Figure 25. Compressibility effects on force and moment variations for centerline tail model at subsonic ($M = 0.4$) and transonic ($M = 0.85$) conditions

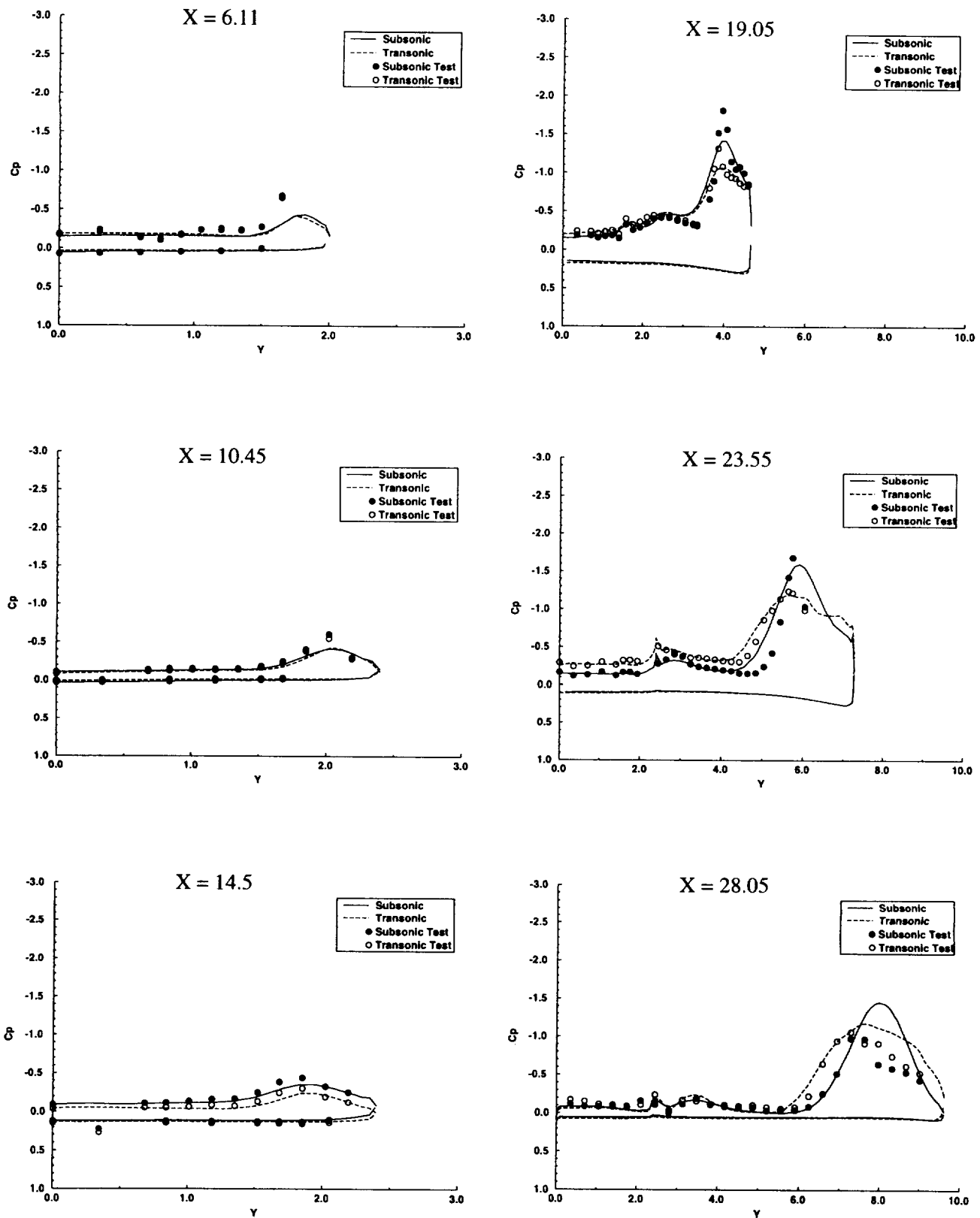


Figure 26. Compressibility effects on surface pressure distributions for centerline tail model, $\alpha = 10^\circ$, subsonic ($M = 0.4$) and transonic ($M = 0.85$) conditions

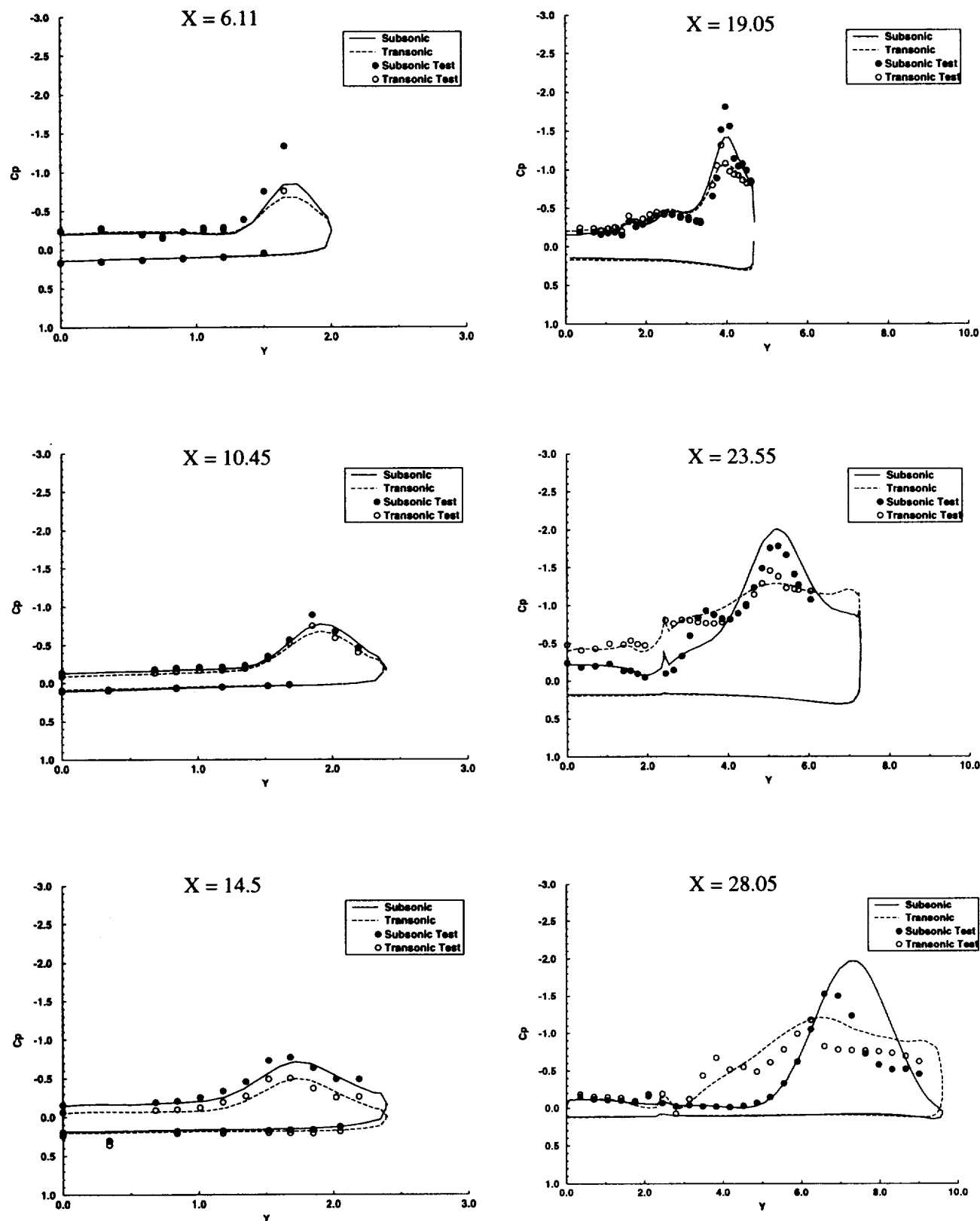


Figure 27. Compressibility effects on surface pressure distributions for centerline tail model, $\alpha = 15^\circ$, subsonic ($M = 0.4$) and transonic ($M = 0.85$) conditions

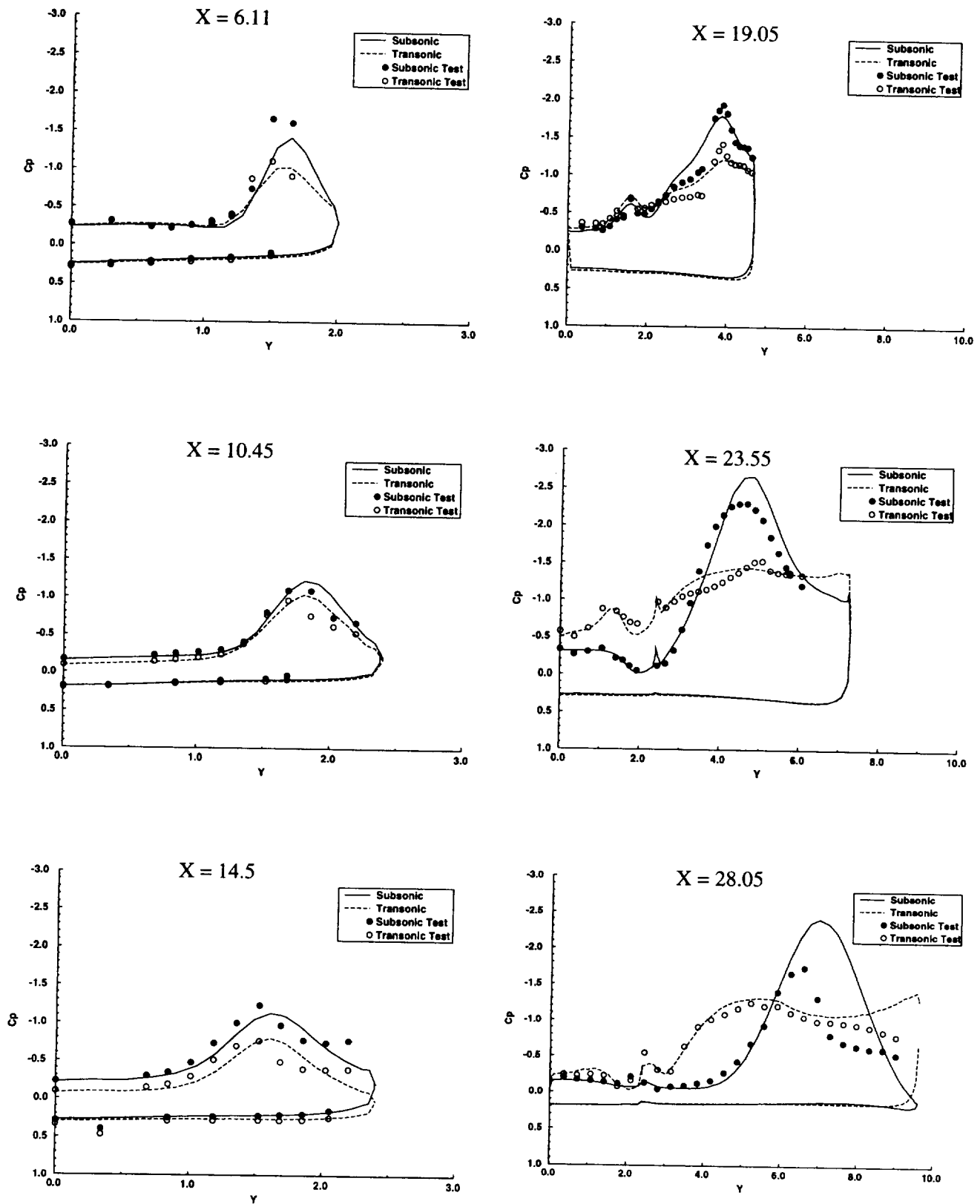


Figure 28. Compressibility effects on surface pressure distributions for centerline tail model, $\alpha = 20^\circ$, subsonic ($M = 0.4$) and transonic ($M = 0.85$) conditions

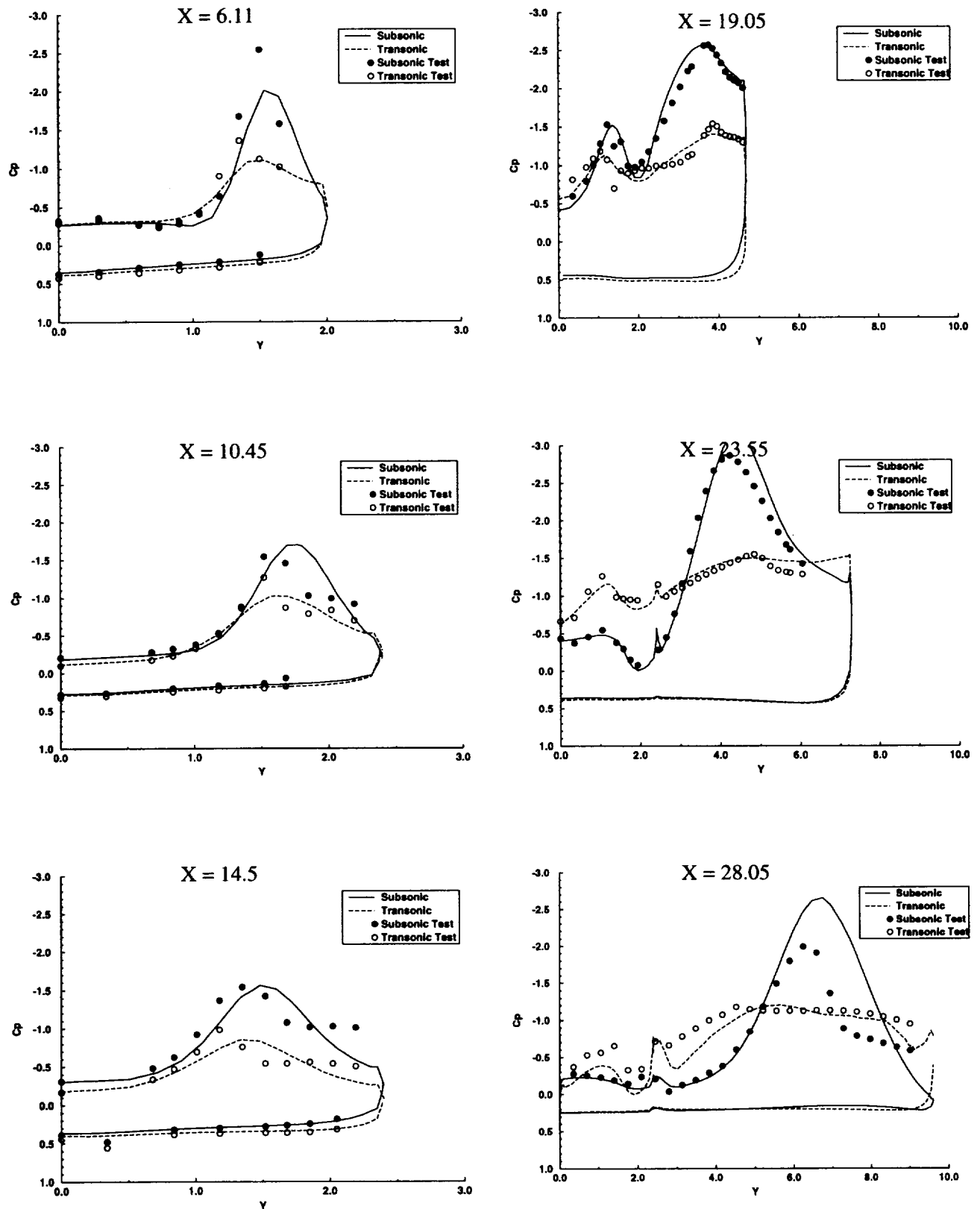


Figure 29. Compressibility effects on surface pressure distributions for centerline tail model, $\alpha = 25^\circ$, subsonic ($M = 0.4$) and transonic ($M = 0.85$) conditions

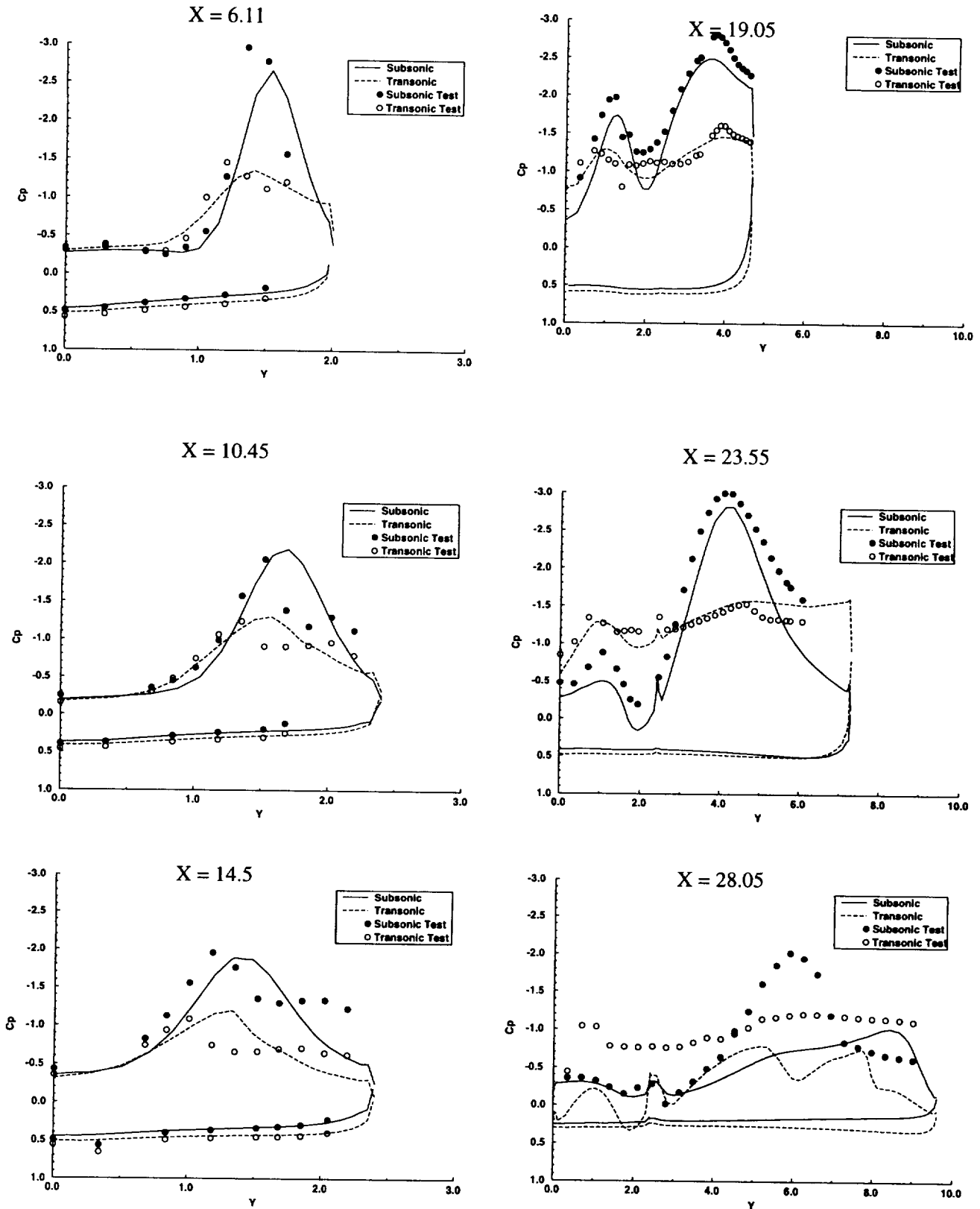


Figure 30. Compressibility effects on surface pressure distributions for centerline tail model, $\alpha = 30^\circ$, subsonic ($M = 0.4$) and transonic ($M = 0.85$) conditions

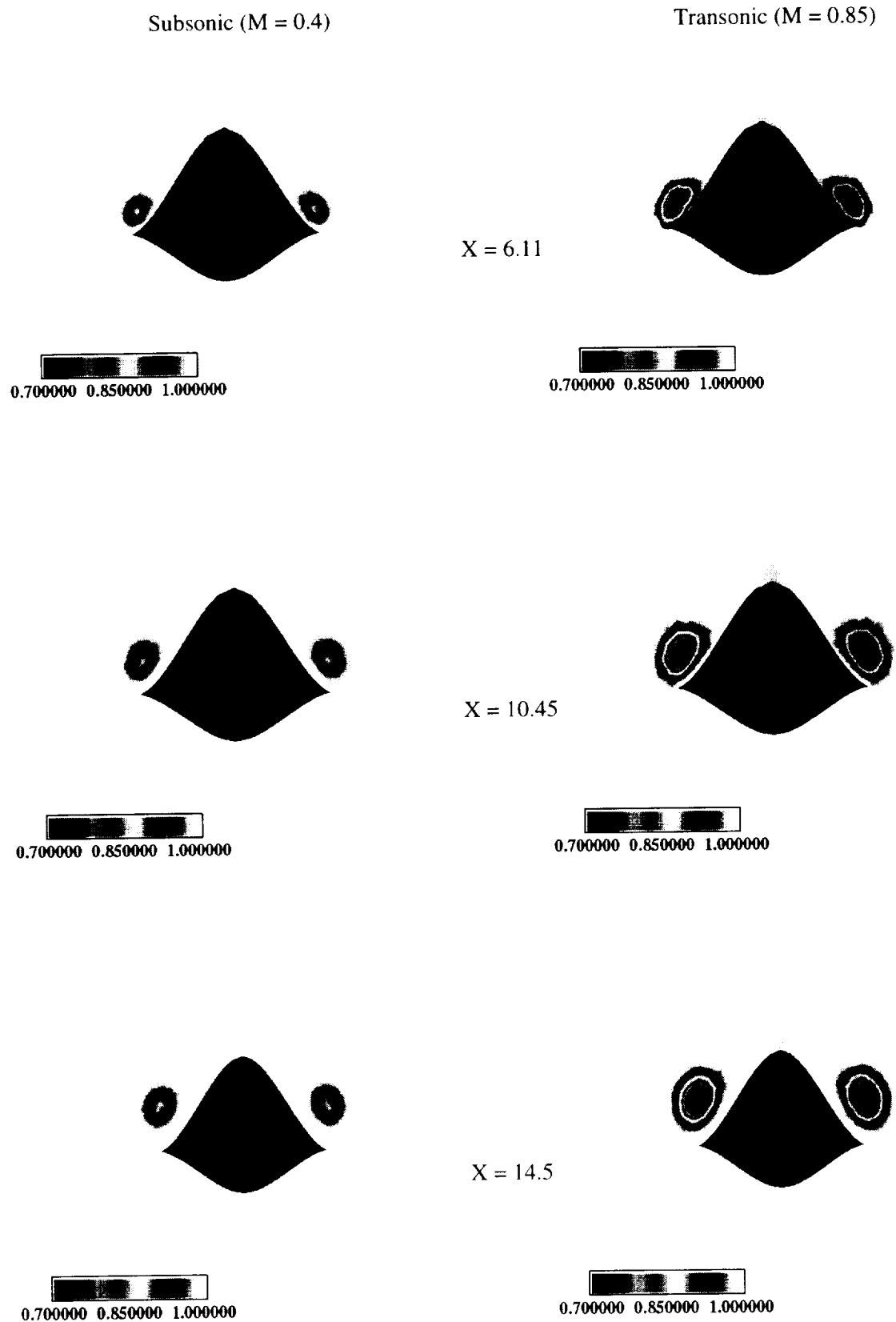
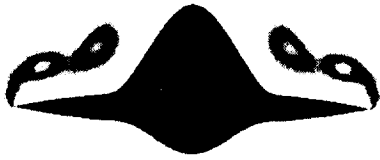


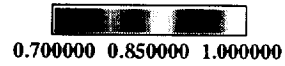
Figure 31. Compressibility effects on off-body total pressure distributions for centerline tail model, forebody stations, $\alpha = 20^\circ$, subsonic (left column) and transonic (right column)

Subsonic ($M = 0.4$)

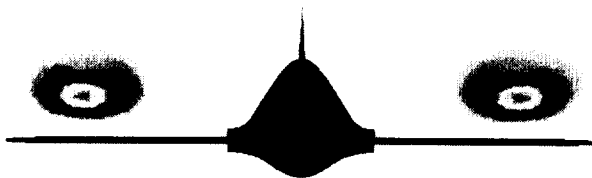
Transonic ($M = 0.85$)



$X = 19.05$



$X = 23.55$



$X = 28.05$

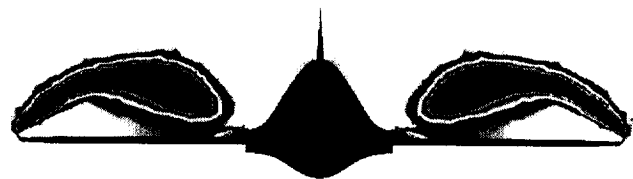
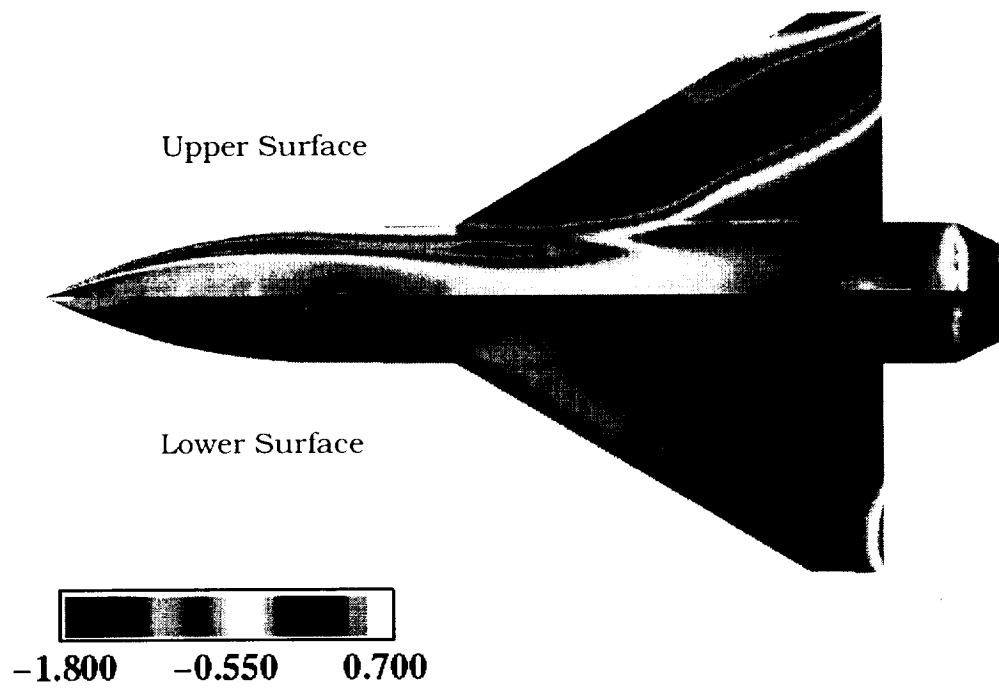


Figure 32. Compressibility effects on off-body total pressure distributions for centerline tail model, aftbody-wing stations, $\alpha = 20^\circ$, subsonic (left column) and transonic (right column)

Subsonic ($M = 0.4$)



Transonic ($M = 0.85$)

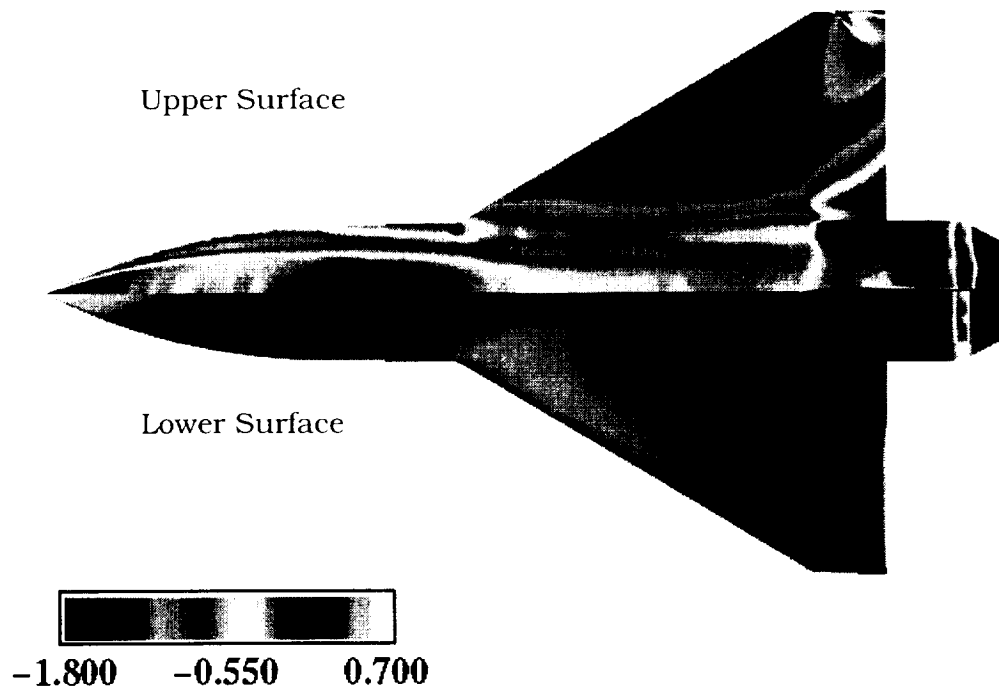


Figure 33. Compressibility effects on surface C_p distributions for centerline tail model, $\alpha = 20^\circ$

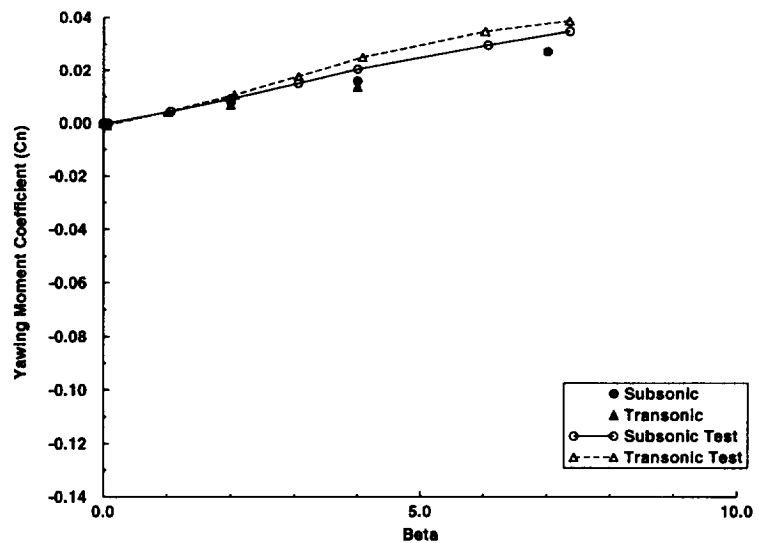
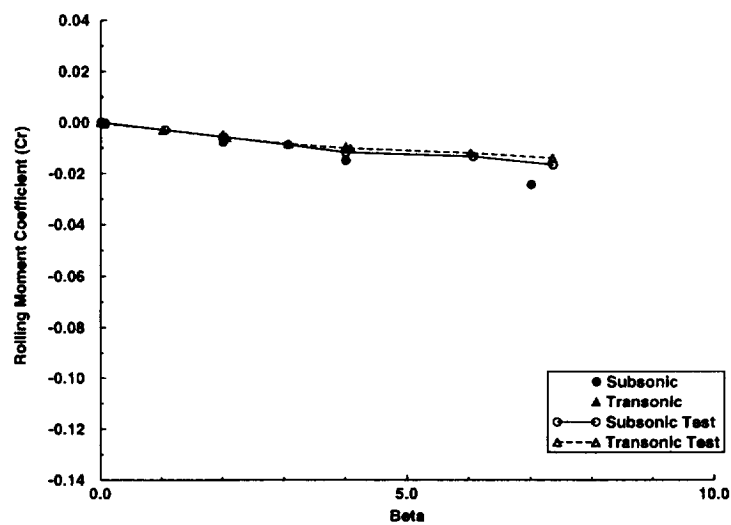
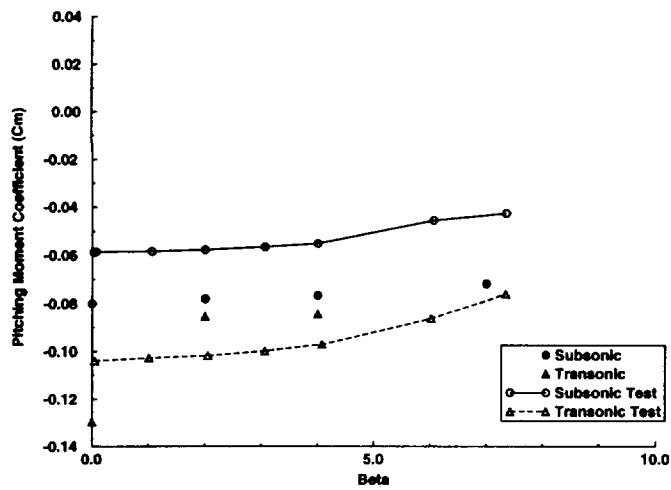


Figure 34. Compressibility effects on moment coefficients in side slip conditions for centerline tail model at subsonic ($M = 0.4$) and transonic ($M = 0.85$) flow conditions, $\alpha = 15^\circ$

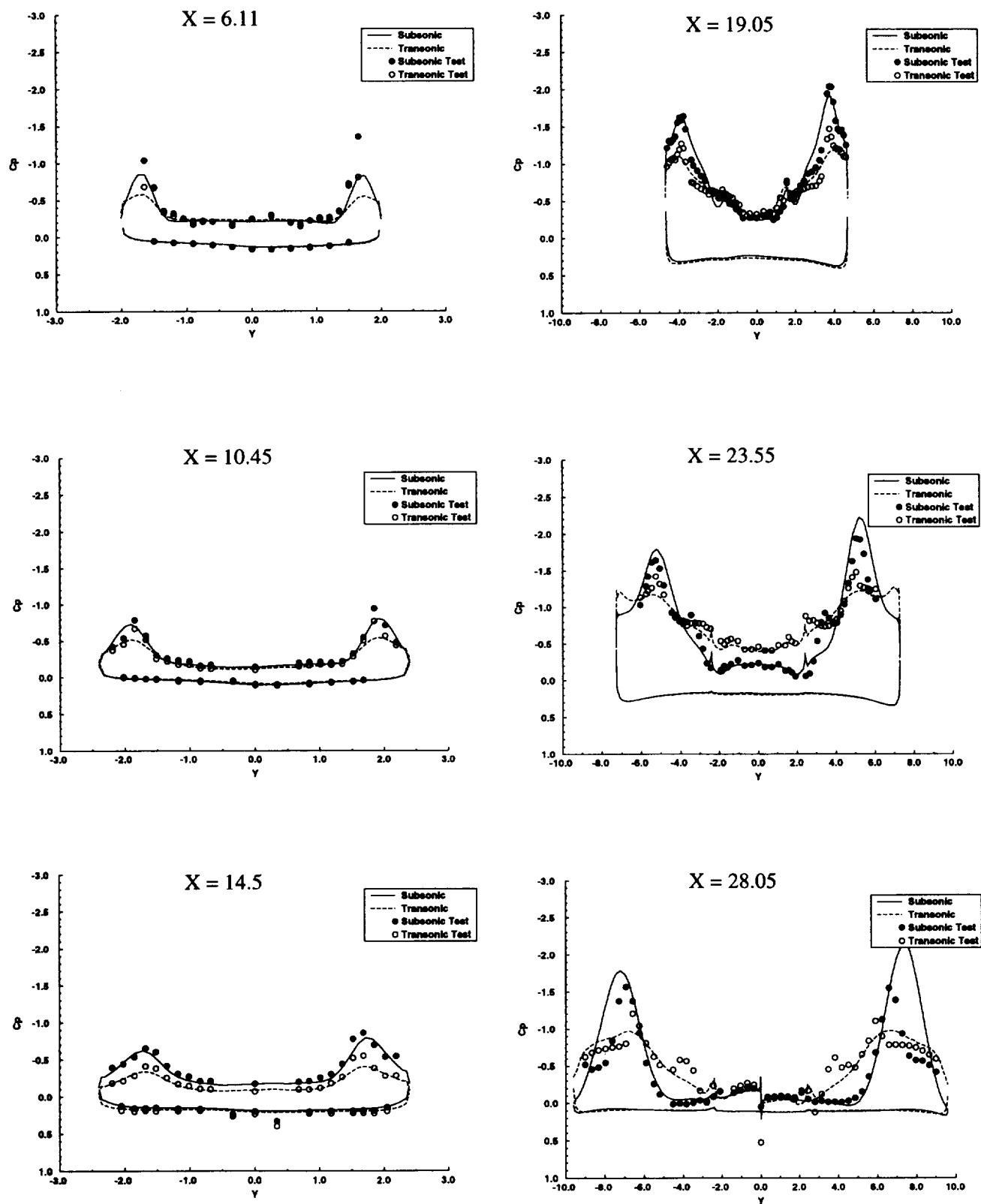


Figure 35. Compressibility effects on surface pressure distributions for centerline tail model, $\alpha = 15^\circ$, $\beta = 2^\circ$, subsonic ($M = 0.4$) and transonic ($M = 0.85$) conditions

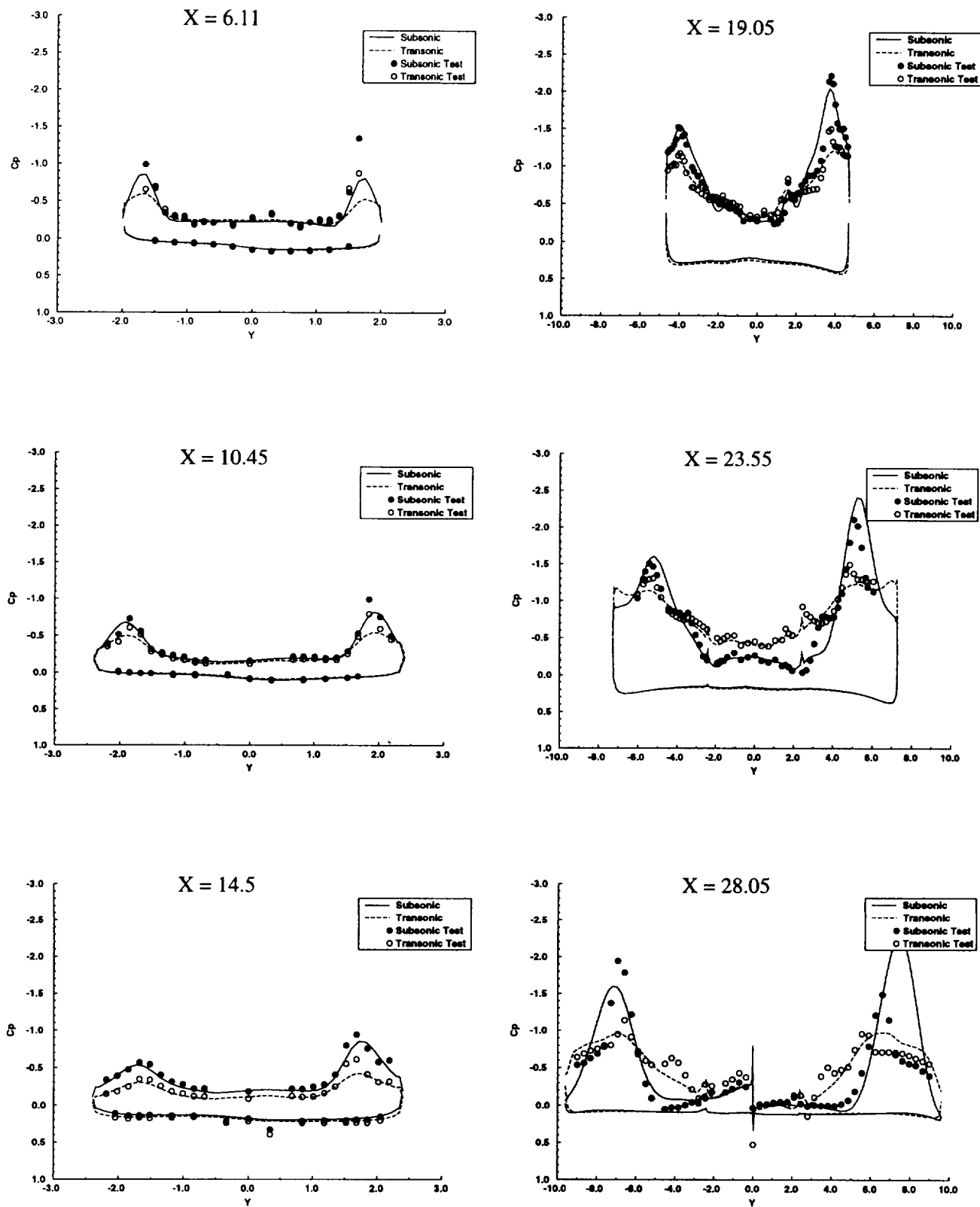


Figure 36. Compressibility effects on surface pressure distributions for centerline tail model, $\alpha = 15^\circ$, $\beta = 4^\circ$, subsonic ($M = 0.4$) and transonic ($M = 0.85$) conditions

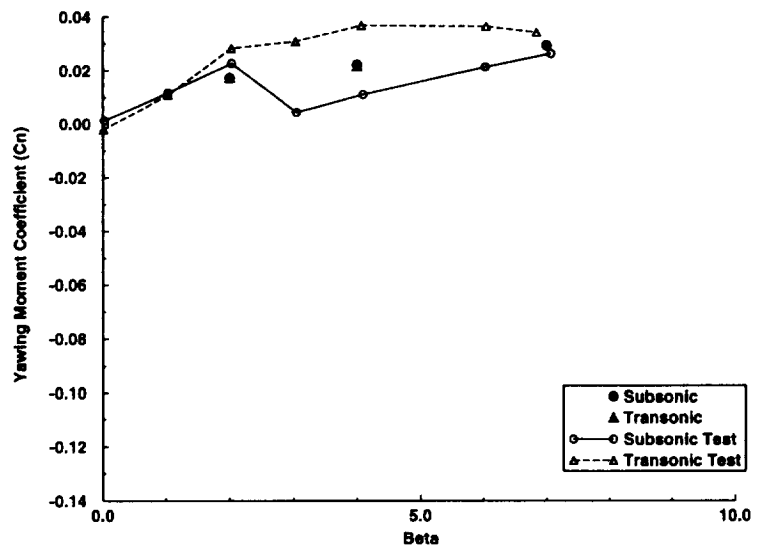
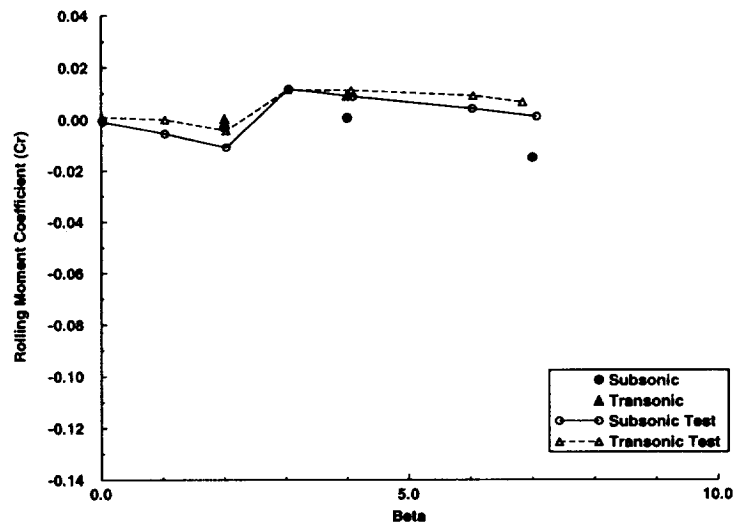
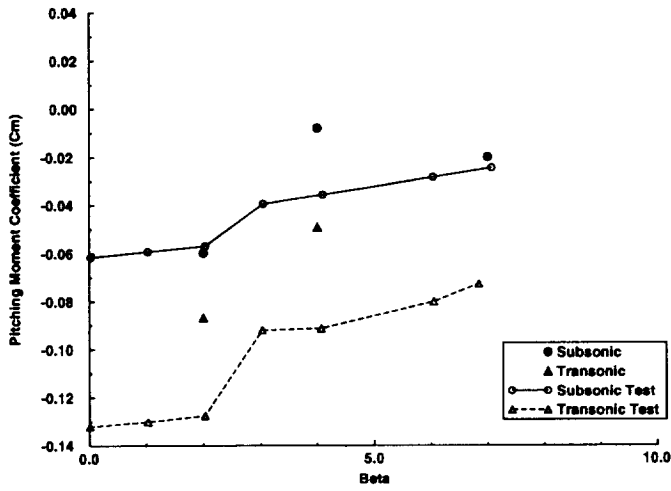


Figure 37. Compressibility effects on moment coefficients in side slip conditions for centerline tail model at subsonic ($M = 0.4$) and transonic ($M = 0.85$) flow conditions, $\alpha = 25^\circ$

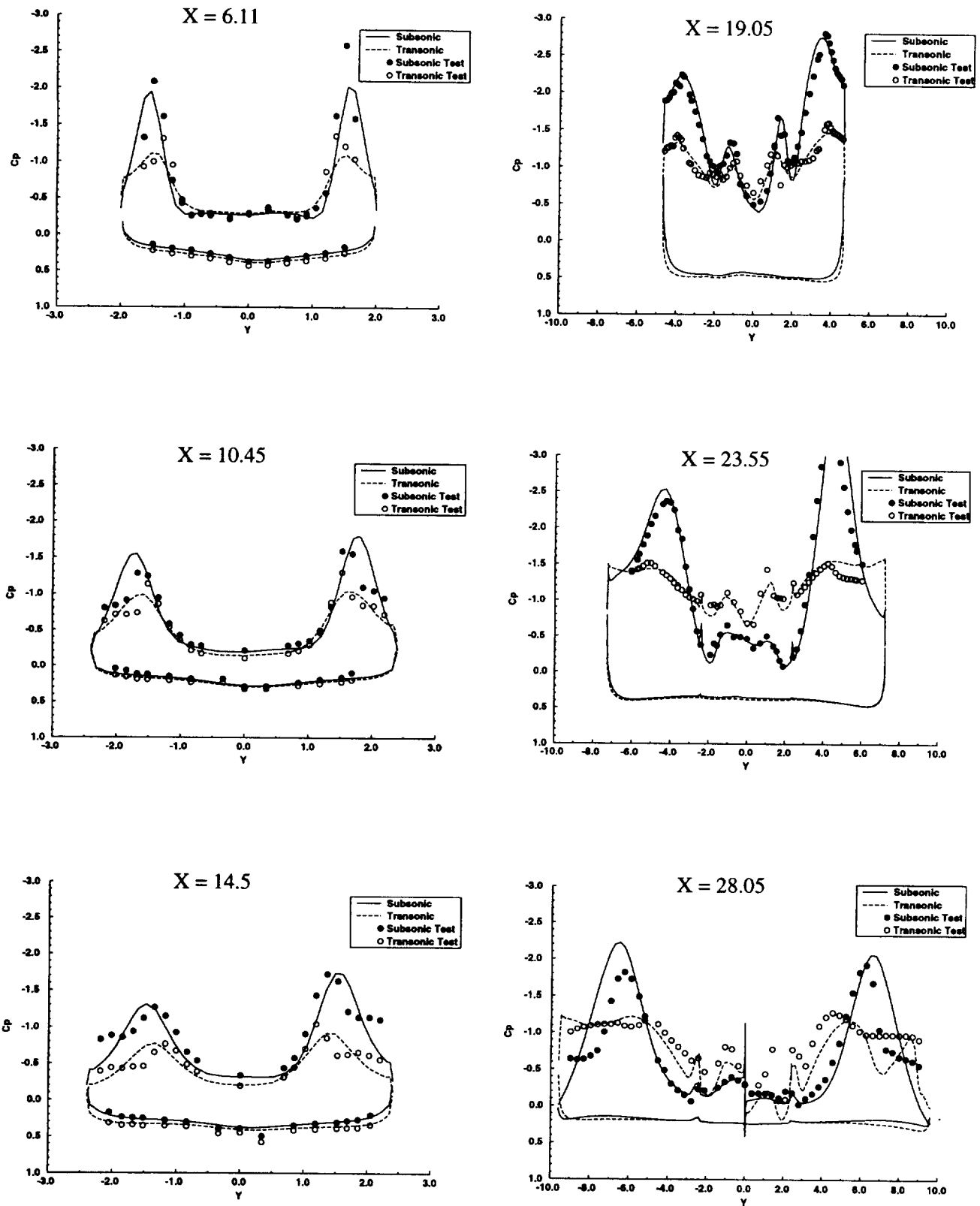


Figure 38. Compressibility effects on surface pressure distributions for centerline tail model, $\alpha = 25^\circ$, $\beta = 2^\circ$, subsonic ($M = 0.4$) and transonic ($M = 0.85$) conditions

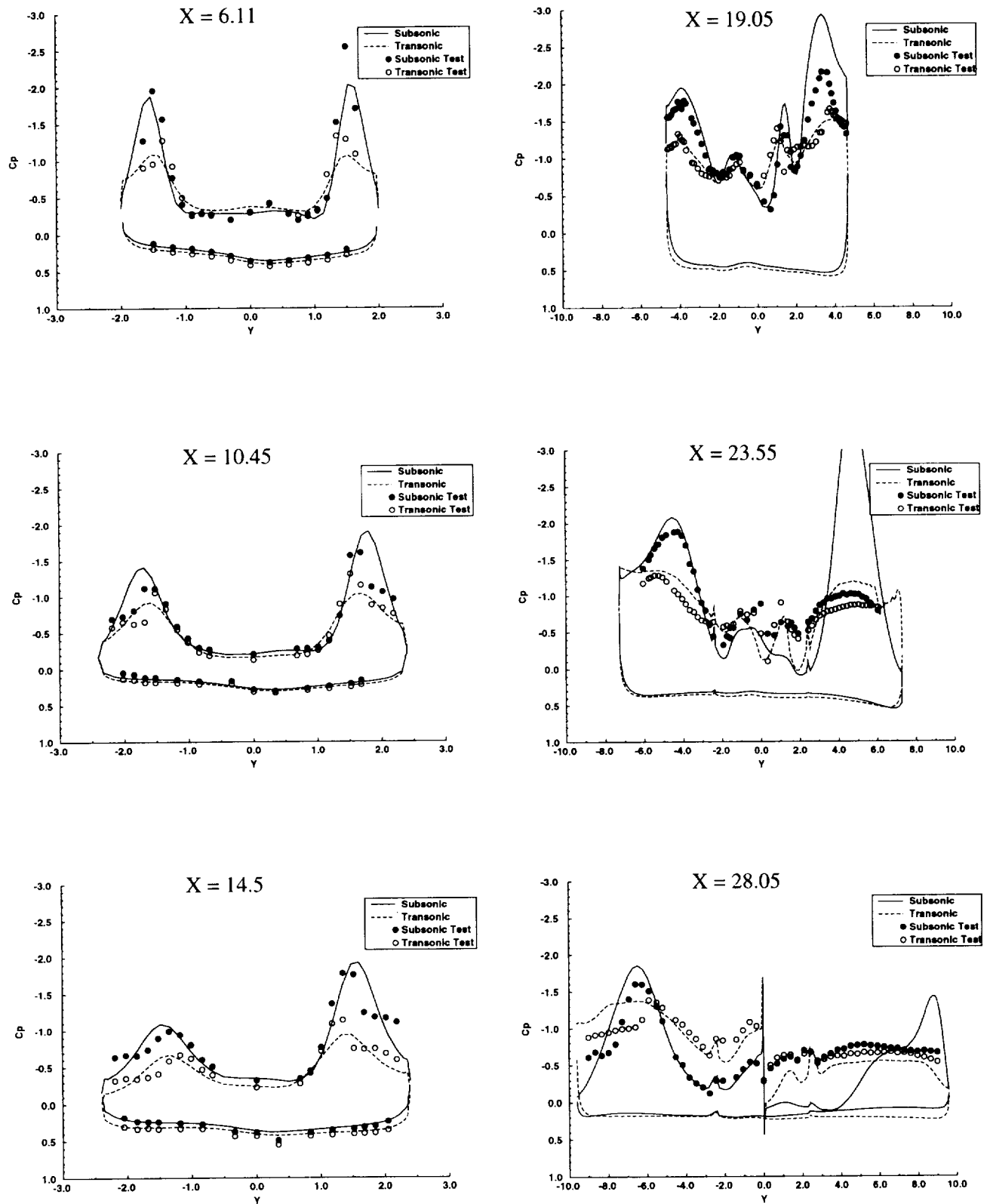


Figure 39. Compressibility effects on surface pressure distributions for centerline tail model, $\alpha = 25^\circ$, $\beta = 4^\circ$, subsonic ($M = 0.4$) and transonic ($M = 0.85$) conditions

Subsonic ($M = 0.4$)

Transonic ($M = 0.85$)

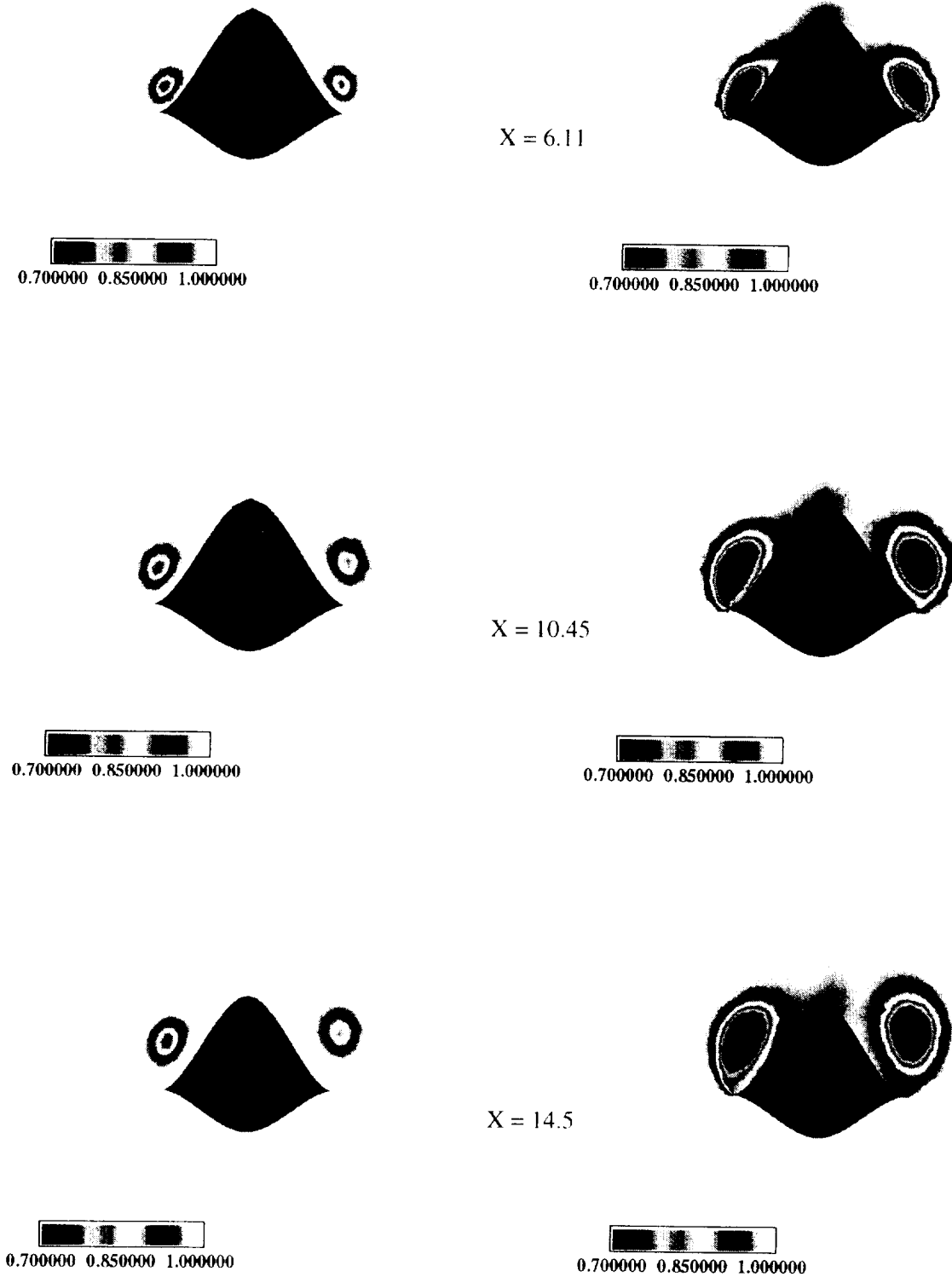


Figure 40. Compressibility effects on off-body total pressure distributions for centerline tail model, forebody stations, $\alpha = 25^\circ$, $\beta = 4^\circ$, subsonic (left column) and transonic (right column)

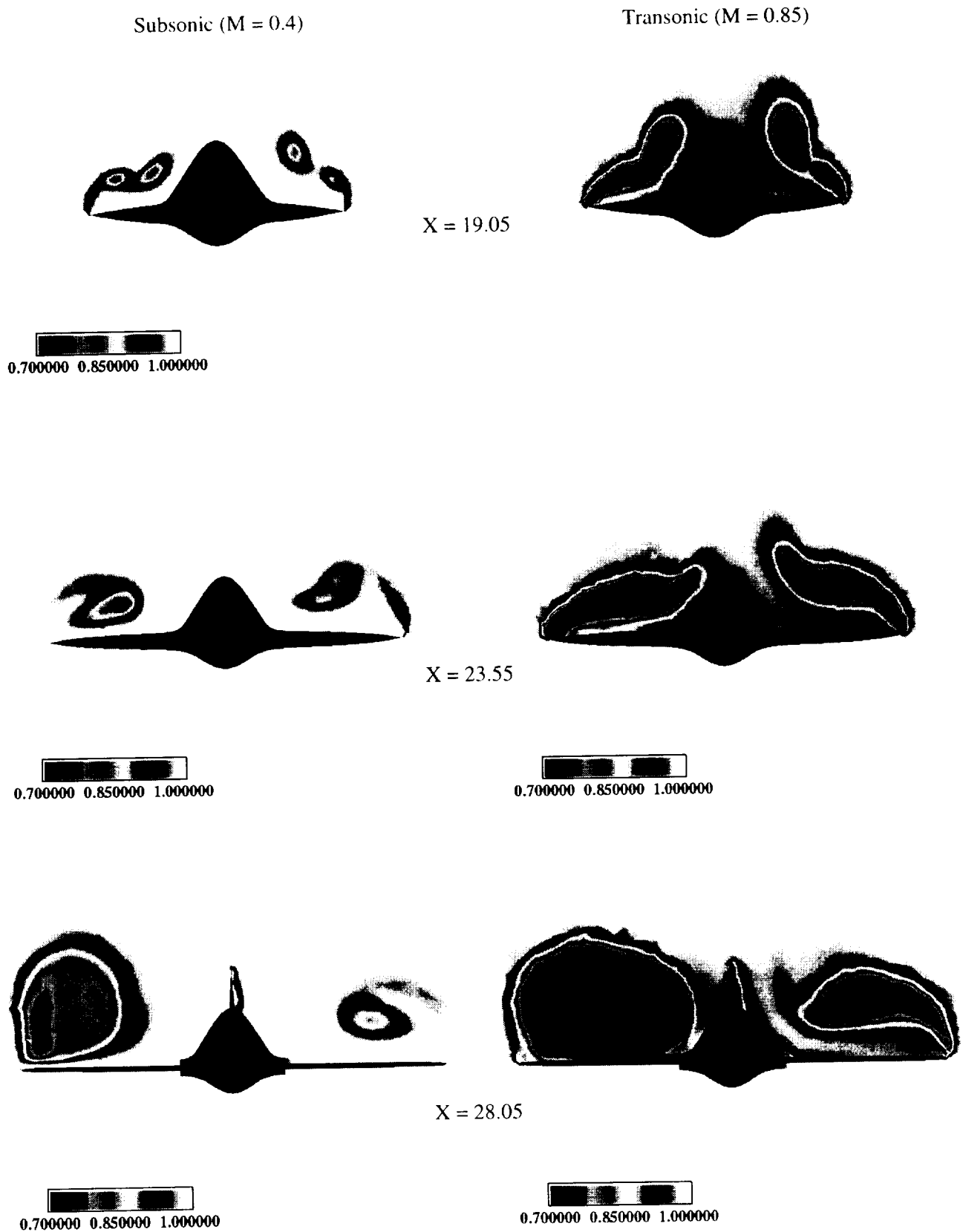
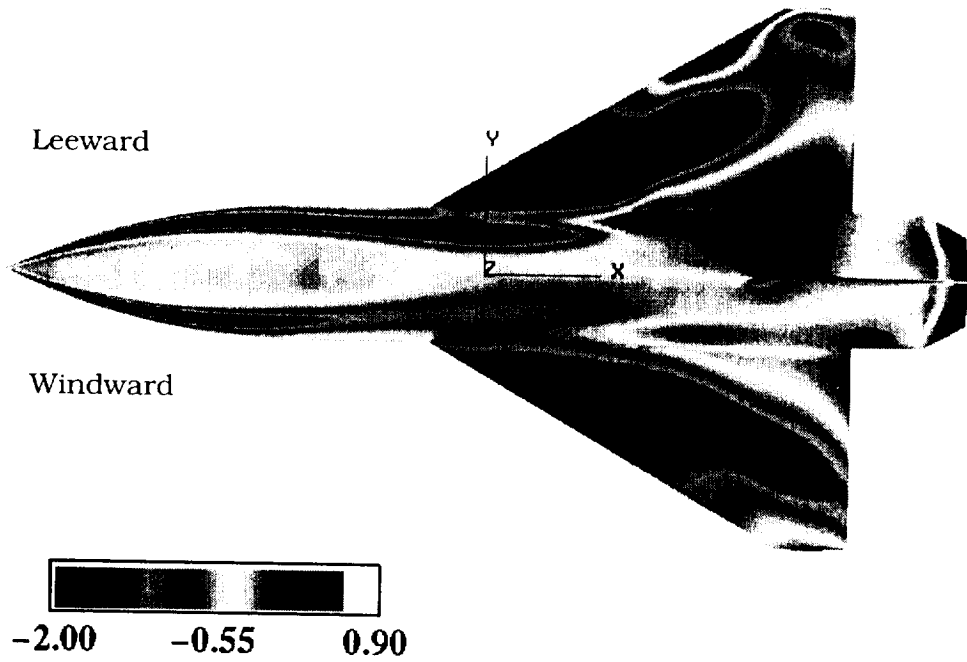


Figure 41. Compressibility effects on off-body total pressure distributions for centerline tail model, aftbody-wing stations, $\alpha = 25^\circ$, $\beta = 4^\circ$, subsonic (left column) and transonic (right column)

Subsonic ($M = 0.4$)
Upper Surface



Transonic ($M = 0.85$)
Upper Surface

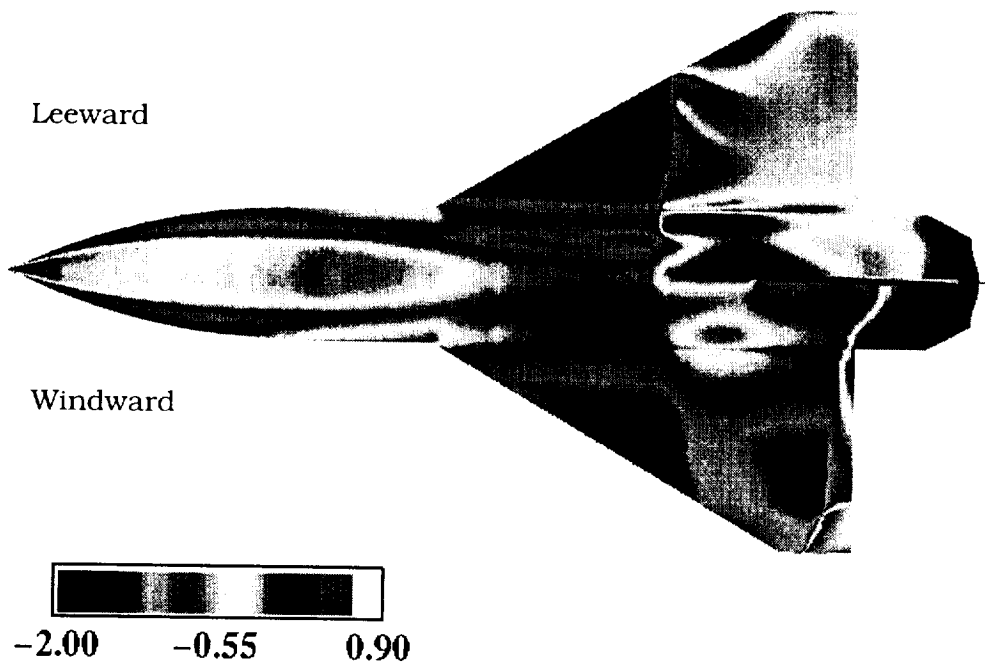


Figure 42. Compressibility effects on surface C_p distributions for centerline tail model, $\alpha = 25^\circ$, $\beta = 4^\circ$

REPORT DOCUMENTATION PAGE			Form Approved OMB No. 0704-0188	
Public reporting burden for this collection of information is estimated to average 1 hour per response, including the time for reviewing instructions, searching existing data sources, gathering and maintaining the data needed, and completing and reviewing the collection of information. Send comments regarding this burden estimate or any other aspect of this collection of information, including suggestions for reducing this burden, to Washington Headquarters Services, Directorate for Information Operations and Reports, 1215 Jefferson Davis Highway, Suite 1204, Arlington, VA 22202-4302, and to the Office of Management and Budget, Paperwork Reduction Project (0704-0188), Washington, DC 20503.				
1. AGENCY USE ONLY (Leave blank)	2. REPORT DATE March 1996	3. REPORT TYPE AND DATES COVERED Contractor Report (2/1/95 to 9/30/95)		
4. TITLE AND SUBTITLE Euler Technology Assessment for Preliminary Aircraft Design - Compressibility Predictions by Employing the Unstructured Grid USM3D Code		5. FUNDING NUMBERS NAS1-19000, Task DA013 WU 505-68-30-03		
6. AUTHOR(S) Tom A. Kinard and Pradeep Raj				
7. PERFORMING ORGANIZATION NAME(S) AND ADDRESS(ES) Lockheed Martin Aeronautical Systems Marietta, Georgia 30063		8. PERFORMING ORGANIZATION REPORT NUMBER		
9. SPONSORING/MONITORING AGENCY NAME(S) AND ADDRESS(ES) National Aeronautics and Space Administration Langley Research Center Hampton, VA 23681-0001		10. SPONSORING/MONITORING AGENCY REPORT NUMBER NASA CR-4711		
11. SUPPLEMENTARY NOTES Technical Monitor: Mr. Farhad Ghaffari NASA Langley Research Center Hampton VA 23681-0001				
12a. DISTRIBUTION/AVAILABILITY STATEMENT Unclassified-Unlimited Subject Category 02		12b. DISTRIBUTION CODE		
13. ABSTRACT (Maximum 200 words) This study has been conducted in support of a NASA project aimed at assessing the viability of using Euler technology to produce aerodynamic data for preliminary design. The primary objective is to evaluate the effectiveness of unstructured-grid techniques in simulating compressibility effects for vortical flows. The approach involves comparing computed subsonic- and transonic-flow solutions with each other and with experimental data for a twin-tail and a centerline-tail modular transonic vortex interaction (MTVI) model, representative of generic fighter configurations. The present effort is focused on the application of the unstructured tetrahedral-grid USM3D code. This code, developed at the NASA-Langley Research Center, employs a cell-centered finite-volume upwind algorithm with explicit or implicit time marching scheme to solve the inviscid compressible-flow Euler equations. In this report, correlations of USM3D solutions with measured data are presented at 0.4 and 0.85 Mach numbers for symmetric as well as asymmetric flow conditions. For symmetric cases, the angle of attack varies from 10 to 30 degrees; asymmetric cases cover side-slip angles of 2, 4 and 7 degrees at selected angles of attack. The results show that Euler solutions can provide meaningful guidelines for preliminary design of flight vehicles which exhibit vortex flows in parts of their flight envelope.				
14. SUBJECT TERMS Computational Fluid Dynamics, Euler/inviscid method, Unstructured grid, Compressibility effects, Sharp-edge flow separation, Vortex flow/burst		15. NUMBER OF PAGES 69		
		16. PRICE CODE A04		
17. SECURITY CLASSIFICATION OF REPORT Unclassified	18. SECURITY CLASSIFICATION OF THIS PAGE Unclassified	19. SECURITY CLASSIFICATION OF ABSTRACT Unclassified	20. LIMITATION OF ABSTRACT	
